2023-05-01

Sensing Optimization of Thermoplastics and Ceramics Fabricated Through Additive Manufacturing

Cory Marquez
University of Texas at El Paso

SENSING OPTIMIZATION OF THERMOPLASTICS AND CERAMICS FABRICATED THROUGH ADDITIVE MANUFACTURING

CORY MARQUEZ

Doctoral Program of Philosophy in Mechanical Engineering

APPROVED:

Yirong Lin, Ph.D., Chair

Tzu-Liang Tseng, Ph.D.

Yifeng Wang, Ph.D.

David Espalin, Ph.D.

Stephen L. Crites, Jr., Ph.D.
Dean of the Graduate School

Dedication

To my parents, who supported me throughout my life. To my mom Josefina who set the standards for me and inspired me to excel in every aspect in life and taught me valuable lessons in life. To my loving family who has always been there for me and supported me along my journey. My grandparents who gave me the opportunity in a life where I could fulfill my dreams and were there for me to raise me. My goddaughter Tiffany, who became a motivation for me to always push myself and be a role model for. The United States Marine Corps, that helped instill discipline in me and helped prepare me for any challenges that life might have and how to improvise, adapt, and overcome. Semper Fidelis.

SENSING OPTIMIZATION OF THERMOPLASTICS AND CERAMICS FABRICATED THROUGH ADDITIVE MANUFACTURING

by

CORY MARQUEZ, M.S.

DISSERTATION

Presented to the Faculty of the Graduate School of

The University of Texas at El Paso

in Partial Fulfillment

of the Requirements

for the Degree of

DOCTOR OF PHILOSOPHY

Department of Aerospace and Mechanical Engineering

THE UNIVERSITY OF TEXAS AT EL PASO

May 2023

Acknowledgements

I wish to thank my family and friends for all their love and support throughout my academic and research years at school. Especially my parents who sacrificed so much for me to helping me reach this milestone in my life.

Secondly, I wish to express my gratitude to my committee chairs, Dr. Yirong Lin for all the guidance, support, and encouragement. Providing me the opportunity to be a part of team and allowing me to learn from you and helped pave the road to my future, will forever be appreciated. Moreover, I would like to thank to my committee members Dr. Tzu-Liang Tseng, Dr. Yifeng Wang, and Dr. David Espalin for proving insightful feedback and mentoring that helped me to fulfill my dissertation expectations.

Thirdly, to my team at Sandia National Laboratory in 8842 department. Thank you for the great support my last two years in my research career. To Dr. Yifeng Wang and Dr. Yongliang Xiong for the mentorship and guidance. To Chris Camphouse for believing in me and continuing to support the decision in keeping me in his team. Also, Jessica Nicole Kruichak, Carlos Miguel Lopez, Amanda Christine Sanchez, and Melissa Marie Mills for being supportive in my time as a year-round intern and guiding me to succeed at Sandia. It is all appreciated.

Lastly, I would like to thank my research team Diana Fontes, Alan Loera, Alan Nuñez, Jesus Mata, Diego Gonzalez, and Annette Baca for their help and friendship over the years. Their devotion at the lab helped us to supersede the expectations in our projects. My colleagues and friends Anabel Renteria, Jaime Regis, Alexis Lopez, Sofia Gomez, Jean Montez, and Sabina Arroyo thank you all for being a part of my journey and success.

Abstract

The objective of this research is to fabricate and optimize thermoplastic and ceramic materials that can be fabricated for Laser Sintering (LS), Direct Ink Write (DIW), and Fused Filament Fabrication (FFF) 3D printing. The fabrication of High-Density Polyethylene (HDPE) thermoplastic particles into spherical allow for better flowability and packing density for LS printing which results in better printability and an increase in mechanical properties. The fabrication of clay ceramic allows the printability application for DIW with the implementation of an embedded wireless temperature and relative humidity sensor. The use of FFF multi-material printing allowed the capabilities of 3D printing a UHF RFID passive sensor with copper (Cu) and zirconium silicate ($ZrSiO_4$) as the primary materials. The use of this material is based on the chemical and thermal properties, along with easy fabrication method, reusability and environmental friendliness.

Table of Contents

List of Tables

List of Figures

Chapter 1: Introduction

1.1 MOTIVATION

The motivation of this research is to use additive manufacturing to fabricate and 3D print high corrosion-resistant thermoplastics, ceramics, and metalloid materials with freedom of design and use of various material properties. The demand of materials with corrosion resistant properties and high temperature resistance is in demand which has led to the desire of fabricating materials to fit the demand. Thermoplastics, ceramics, and some metallics have great corrosion resistance properties that can withstand high temperatures, as well as have suitable mechanical properties that make them ideal for uses in harsh environments in various industries. For this reason, efforts are made to make materials applicable for specific forms of additive manufacturing as well as capabilities of uses for embedded sensing of thermal readings. This dissertation aims to fabricate thermoplastic to be applicable for Laser Sintering and test the mechanical properties. It also aims in embedded thermal sensors in clay ceramic using Direct Ink Write 3D printing and multi-material printing copper and zirconium silicate through Fused Filament Fabrication 3D printing.

1.2 Background

Thermoplastics are a type of plastic polymer materials that is able to be molded at specific temperatures and solidify upon cooling. Ceramics are hard yet brittle materials that are easy to fabricate and 3D print and post-process. Metallic materials have high thermal conductivity and great corrosion resistance properties and are typically ductile and malleable. Various respectable industries use these materials for every day uses such as aerospace, industrial, and nuclear fields due to unique properties such as recyclability, corrosion resistance, high thermal resistance, and easy fabricable features that make them feasible for additive manufacturing.

1.2.1 Thermoplastics, Metallic, and Ceramics

Primary materials that will be discussed in the dissertation include high-density polyethylene (HDPE) as a thermoplastic, porcelain 5 clay and zirconium silicate ($ZrSiO_4$) as the ceramics, and copper (Cu) as the primary metal. HDPE is a polyethylene thermoplastic made from monomer ethylene and is a semi-crystalline material and is recyclable. Porcelain 5 clay is an inorganic material that is easy to fabricate and post-process and is an environmentally friendly reusable material. $ZrSiO_4$ is a ceramic that is a silicate of zirconium and is a hard and dense material. Copper is a ductile material that is found in the free metallic state in nature and is also a soft and malleable material.

High corrosion resistance and thermally stable materials

The HDPE offers a superior corrosion resistance and higher working temperature range compared to standard polymers. These materials chemical resistance makes them ideal materials for harsh environment fields in substitution of other materials because of it. Both clay and $ZrSiO_4$ are ideal materials for use in harsh environments due to their high resistance to corrosion properties and due to not wearing down as other non-ceramic materials. These two ceramics are also more thermally stable, making them of higher demand in use for different applications. For Cu, this metal is nearly immune to corrosion due to its natural protective film that forms on the surface and also has excellent heat resistant properties which makes them the preferred metal for extreme temperature environments.

1.2.2 Additive Manufacturing

Additive manufacturing (AM) which is normally referred to as 3D printing, is a technology for rapid prototyping in order to fabricate three-dimensional parts that are designed through computer aided design (CAD) software. Per the American Society for Testing Materials (ASTM)

F2792-12a defines the seven classifications for AM, specifically Binder Jetting (BJ), Directed Energy Deposition (DED), Material Extrusion (ME), Material Jetting (MJ), Powder Bed Fusion (PBF), and Vat Photopolymerization (VP). AM allows the capabilities to use wide range of materials and allowing the ability of freedom of design printing.

Various forms of AM technologies are available for printing these materials as shown illustrated in Figure 1.1. PBF and LS is a user-friendly option to print complex designs with little feedstock preparation. The limitation to this technology though is it requires the use of only micro size particles within a preferred range of 20-80 μm with materials density decrease after post-process (≈ 60 % Theoretical Density). Two forms of ME include fused filament fabrication (FFF) and direct ink write (DIW). While DIW allows fabrication of high-dense ceramics (≈ 80-90 % Theoretical Density) with larger selection of applicable materials. A limitation to this form of technology includes typical low resolution and constraints in freedom of design due to the printing technology. Lastly, FFF technique offers a wider selection range of materials applicable for printing with higher density (≈ greater than 90 %). However, the current limitation to this is poor resolution and rough surface finishes.

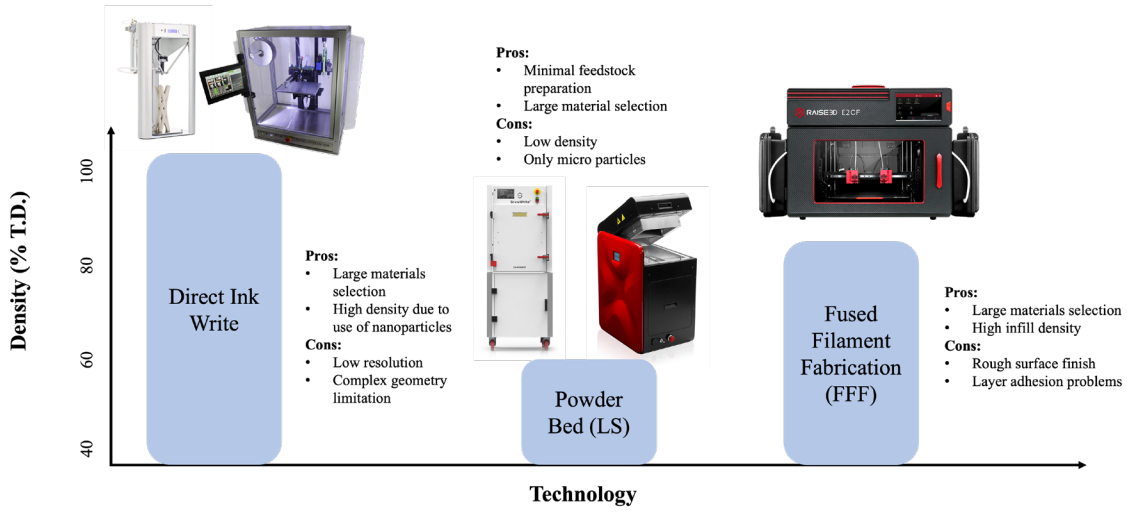

Figure 1.1: Additive Manufacturing Technology for thermoplastics, ceramics, and metals.

Laser Sintering Technique

Laser sintering (LS) is a form of PBF technology that uses a high-power laser to sinter micro size particles polymer powders into a solid structure based on the designed 3D model. The main advantage of LS printing is the ability to print high complexity build parts without the use of inner supports as the compacted powder bed acts as its own support. This allows for extreme detailed prints with high dimensional accuracy. A drawback to this form of printing is a limitation in raw materials suitable for LS printing LS powder must meet standards in order to be applicable for LS printing which requires specific fabrications methods that do not decrease properties of the materials during the process.

Direct Ink Write Technique

DIW printing consists of the fabrication of a slurry material to be extruded through a nozzle either through pressure or a piston, which is then deposited onto a substrate surface for a layer-to-layer print. An advantage of DIW 3D printing is the ability for room-temperature deposition of

materials to print various complex prints. A main drawback of this form of printing is the required initial pressure to initiate the print and continuously dispense the material to avoid improper material flowability and deposition.

Fused Filament Fabrication Technique

FFF is an AM process in which desired material is pushed through a heated nozzle to create objects by layer-to-layer deposition. Main advantages of this form of AM are the large selection of materials usable for this form of printing that allow the ability for large object printing and easily scalable. This form of technology also allows the use of multi-material printing concurrently. A drawback to FFF printing is low resolution prints which make small prints unideal and printed parts typically have rough surface finishes.

1.2.3 Dissertation overview

This dissertation is structured as follows. Chapter 2 begins by fabricating HDPE non-spherical particle powder into spherical particles through melt-blend extrusion and characterize the fabricated powder for LS printability by viewing the morphology, testing powder flowability, and packing density. Chapter 3 will be establishing the optimal printing parameters of the spherical HDPE particle powder using DSC to calculate the sintering window and testing the mechanical strengths through tensile testing and see how the crystallinity percentage factors into the strengths using XRD to characterize the crystallinity. Chapter 4 introduces porcelain 5 clay with established fabrication water-clay mixing ratios to make printable slurry to print various shapes and apply that with an embedded wireless temperature and relative humidity active sensor and conduct thermal tests. Lastly, chapter 5 uses multi-material printing to embed a wireless passive UHF RFID temperature and relative humidity sensor within zirconium silicate layers enclosed with a copper

outer structure and test sensing accuracy and distance as well as compression tests to evaluate multilayered mechanical strengths.

Chapter 2: Fabrication of High-Density Polyethylene Spherical Particles for Laser Sintering Additive Manufacturing

This chapter describes the implementation of using melt-blend extrusion (MBE) as a form to reshape HDPE non-spherical particles to spherical shapes. By establishing a mixing ratio between HDPE and using polyethylene glycol (PEG) as a water-soluble matrix and mix the two immiscible materials at established extruding parameters. The extruded material is quenched at room temperature in water to also allow the matrix to dissolve to leave HDPE powder by itself. Different mixing ratios of HDPE wt. % allowed to control the particle size range as desired. Literature suggests that spherical particles are the desired particle shapes for LS printing as it allows better flowability of the powder and increases the packing density with the control of a range of particle sizes in order to reduce or eliminate porosity during printing. Therefore, the fabricated spherical particle powder is evaluated for LS printability based on powder flowability, particle size range, and packing density. This study proves the feasibility of using MBE with two immiscible materials to fabricate spherical particles for LS printing.

2.1 Introduction

Additive manufacturing (AM) is a growing industry that has allowed rapid production of materials with rapid prototyping, low cost of production, and distributed manufacturing in various fields of applications such as aerospace, biomedical, industrial, and other respectable fields of study [1]. In the AM industry there are seven forms of 3D printing methodologies which include Material Extrusion, Directed Energy Deposition (DED), Binder Jetting, Powder Bed Fusion (PBF), Sheet Lamination, Material Jetting, and Vat Photopolymerization [2]. One of those methods for PBF is Laser Sintering (LS), which consists of a powder bed as a self-support system,

which is commonly used for printing polymer powder materials with complex geometric shapes [3]. During the printing process, a laser beam is used to melt or fuse polymer particles in a layer-by-layer deposition while the powder bed acts as its own self-support system [4]. One of the LS setbacks is the limited availability of printing materials which is due to the irregular morphological shape of the particles and the desired particle size range of 10-100 μm [5], which are required to assure printability. Typical available materials for LS printing are polyamide powders, yet the desire for wider selection of materials such as polypropylene and polyethylene are required [6]. Thermoplastics are of high interest due to their thermal and chemical properties [7], which makes them desirable in various industries such as aerospace and automotive. The current setback with using thermoplastics for LS applications is the available morphology of the particle shapes, which have shown to be non-spherical, leading to flowability and printability complications and thus making them with poor mechanical properties [8]. A recent approach to make thermoplastics SLS applicable have been through the fabrication of semi-crystalline spherical particles that would improve flowability, printability, and packing density of the selected material [9]. Currently, some methods that are used to change the morphology of powder include Thermally-Induced Phase Separation (TIPS) and Melt-Blend Extrusion (MBE).

TIPS method involves a liquid-liquid phase separation (LLPS) and crystallization to create porous membranes that allow the creation of polymer microspheres through the dissolution of the polymer in a solvent [10]. Wang et al. studied the TIPS with polypropylene (PP) with various solvents and the effects on their morphology to create spherical particles[10]. Wang et al. applied TIPS method to create near-spherical polyetheretherketone (PEEK) particles with embedded carbon nanotubes (CNT) with the desired particle size and size distribution for SLS application [11]. Hejmady et al. used the method to prove its versatility of it with various thermoplastic

polymers such as PP, low-density polyethylene (LDPE), polystyrene (PS), polyamide 12 (PA12) and PA12 filled with CNT [12]. This method showed both, the ability to create spherical particles and the versatility towards different polymers. However, the TIPS method has limitations as it requires multiple time-consuming processing stages and has limited potential of fabrication scaling up. In addition, TIPS method can suffer from poor control over the diameter distribution of the fabricated particles, and the spheres often stick to each other during formation and can result in large agglomerations [13]. Additionally, the use of solvents required to fully dissolve thermoplastic powders results in a time-consuming process that requires the use of harsh chemicals dependent on the material.

On the other hand, MBE or hot melt extrusion (HME) has been a popular method of approach for creating spherical particles by melt blending immiscible materials to create a transparent filament and then dissolving the matrix to be left with just one single material [14]. Kleijned et al. applied this method by melt blending polybutylene terephthalate (PBT)/polyethylene glycol (PEG) to create spherical particles using a single-screw extruder and then dissolving the matrix and extracting the PBT particles for SLS printing [5]. Drummer et al. discussed the path of the morphological development structure of PA12-PEG and PA12-PVA through the phase changes [15]. Yang et al. investigated the properties of PA12/PEO blends with different viscosity ratios to control the particle size range and the average diameter size [16]. Zhou et al. implemented a melt spinning Plateau-Rayleigh through molten PA12/PEO fibers at high temperatures to create near-spherical particles and investigated the ability to get the desired morphology at a faster time [17]. A drawback to this method is the high energy input coming from the applied shear forces and high temperature, which could lead to polymer degradation and thus significantly impact the product quality [18]. However, this method has shown to be consistent in

creating spherical particles with polymers that are intended for LS printing and is applicable for thermoplastics.

This work presents the application of MBE with HDPE to reshape irregular thermoplastic particles into spherical particles, which will be suitable for LS printing with improved printability. The change in morphology of produced HDPE powder can be confirmed by Scanning Electron Microscopy (SEM). Here, the use of PEG at different mixing ratios was investigated to determine the influence of controlling the particle size and size distribution while being able to dissolve the PEG matrix with pure HDPE confirmed by Fourier Transform Infrared Spectroscopy (FTIR). The particle size was investigated to see the influence of different concentrations of HDPE with different mixing ratios. Finally, flowability and packing density tests were conducted to compare with the irregular HDPE powder to confirm improvement in the fabricated HDPE printability properties.

2.2 Experimental details

2.2.1 Materials

High-Density Polyethylene (HDPE) (AXALTA Coathylene® Fine Powders; average particle size 40-60 μm; density of 0.951 g/cm^3) powder was used as the primary thermoplastic material for the fabrication of spherical particles. Polyethylene glycol (PEG) (Sigma-Aldrich; upper melting range ≤ 67 °C; molecular wight of 35,000 g/mol) flakes was used as the matrix.

2.2.2 MBE Fabrication Process

HDPE powder was melt-blended with PEG flakes of ratios consisting of 10/90, 20/80, 30/70 wt. % with 50 g total respectively. A co-rotating twin-screw extruder Process 11 (Thermo Scientific, Karlsruhe, Germany) with a barrel temperature profile of 50, 50, 105, 105, 129, 175, 175, 175 ºC from feeder zone to die zone respectively was used to melt blend the powder mixtures.

The screws had a 11 mm base diameter with a L/D 40 with a 1.5 mm die nozzle. The material was deposited into a feeder chamber at a feed speed of 10 RPM and a screw speed of 50 RPM. Transparent filament was extruded out from the die which signified fully melted material. The filament was then dropped immediately into a beaker of 300 mL of water to allow immediate dissolvement of the PEG matrix. Water was preheated to 80 ºC and kept at a constant magnetic stirring speed of 450 RPM to help dissolve the PEG matrix completely and retain HDPE powder. The sample was kept at 80 °C for 2 hours, followed by magnetic stirring for 12 hours at room temperature, afterwards the water solution was filtered using a metallic mesh with a mesh size of 25 µm. A vacuum filtration (Filtr8 Labs) system was used to filter the water phase from the HDPE powder. A second cycle was done with clean water with same parameters to remove any remaining matrix on the surface of the particles. The samples were then placed in a vacuum oven (Lab Companion) at 40 ºC for 12 hours to properly dry the powder. A motor and pestle system were used to break the dried powder and reduce agglomerations of particles. Figure 2.1 demonstrates the overview steps from the extrusion process, rinsing cycles, and powder extraction process.

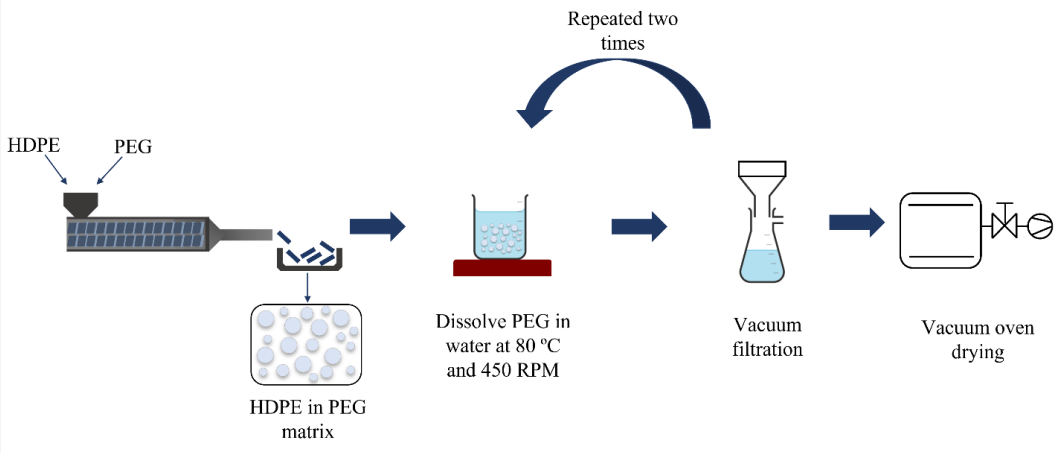

Figure 2.1: Schematic illustration of the overview of the spherical particle production of HDPE.

2.2.3 Material Characterization

Scanning Electron Microscopy (SEM) imaging was performed to characterize the morphology of HDPE using the IT 500 LV Scanning Electron Microscope (JEOL USA, Inc., Pleasanton, CA, USA). A 108 Auto/Se Sputter Coater (TED PELLA, Inc., Redding, CA, USA) was used to perform sputter coating to create a conductive layer of gold metal on the sample in order to inhibit charging, reduce thermal damage, and improve secondary electron signal which is required for topographic examination for SEM. For the gold sputtering, nitrogen flow was set to 0.3 psi, and approximately 10 nm. Thermogravimetric analysis (TGA) was performed using a TGA 55 (TA Instruments, New Castle, DE, USA), which was used to determine the thermal degradation of as-received HDPE and PEG flakes for the maximum heating zone temperature. The sample was heated at a temperature range from 25-550 ºC with a ramp rate of 10 ºC/min in an atmospheric air condition [19]. To determine the middle temperature zones for MBE and successfully melt the immiscible materials a differential scanning calorimeter (DSC) test was performed using a DSC 404 F1 Pegasus (NETZSCH). The DSC was also used to calculate the percentage of crystallinity based upon the melting enthalpy areas of the temperature of crystallinity and melting temperature. The samples were tested from room temperature to 200 ºC with a heating rate of 5 ºC/min and cooled down at the same rate. The viscosity of HDPE/PEG at different mixing ratios was decided using a DHR-2 rheometer (TA Instruments, New Castle, DE) with a parallel plate geometry using a 2.5 mm gap distance [16]. The test was performed using a flow sweep at 175 °C based on the maximum temperature zone set through the MBE process. Particle size analysis and distribution tests is used to determine the average particle size of HDPE powder with the standard deviation. The test was performed using a MICROTRAC S3500 and MICROTRAC SDC (Microtrac, Montgomeryville, PA) to obtain the particle size analysis. The powder was placed in the SDC with distilled water, which then pumps the sample into the S3500 which uses a laser to scan the particles. Powder flowability was performed to compare with the received HDPE powder and the spherical HDPE powder to analyze the angle of repose. A PF1 (SOTAX, Westborough, MA)

flowability tester was used to analyze the angle of repose for the powder to evaluate the flow properties. A Fourier Transform Infrared Spectroscopy (FTIR) for post-processed HDPE specimens to confirm dissolvement of PEG matrix. This data was recorded through a Fisher Scientific NICOLET iS5 Spectrometer (300 Industry Drive, Pittsburgh, PA, USA).

2.3 Results and Discussions

2.3.1 Melt Blend Extrusion

Three different mixing ratios were selected to study the ability to control the particle size while still being able to create spherical particles for 10/90, 20/80, and 30/70 wt. % HDPE to PEG respectively. This was determined as these three mixing ratios showed complete dissolvement of the PEG matrix in comparison to higher HDPE mixing concentrations where HDPE filament was left with little PEG dissolvement. A total amount of 50 g was used for each mixing ratio for melt blending in order to retain sufficient amount of HDPE powder for analysis. TGA was conducted to determine the maximum temperature allowed for melt extrusion and the thermal degradation of HDPE and PEG. Figure 2.2 shows that PEG starts degrading at around 178 ºC, therefore 175 ºC was determined to avoid any degradation of PEG during the process. A TGA on virgin HDPE showed that at 175 °C, HDPE residual weight % was at 99.901% making it a suitable temperature to melt the immiscible materials. To view the viscosity of the melt blends of the immiscible materials at the final set temperature at 175 °C rheological measurements were obtained. Tests were conducted for virgin HDPE, PEG, and the mixing ratios to determine the rheological behavior of the different melt blend compositions during the MBE methodology. In Figure 2.3, it is seen that the viscosity for PEG and melt blend mixtures showed a Newtonian behavior while virgin HDPE powder showed a non-Newtonian behavior throughout. HDPE has a high inter-chain entanglement density that results in extremely high melt viscosity; thus, its molecules are difficult to move while being melted. The high molecular weight of HDPE can lead to long molecular chains [20] which can typically tend to aggregate and make it difficult to stretch or flow at the

temperature even higher than the melting point which attributes to HDPE showing a non-Newtonian behavior. On the other hand, addition of amount of PEG can improve the extrusion behavior of HDPE, since the pressure vibration and wall-slip do not occur, therefore the extrusion behavior of the HDPE particles change becoming easier to extrude. The change on the rheological properties of HDPE-PEG powder mixtures is due to the high content of PEG flakes, which mainly affects the amorphous fraction of HDPE, reducing the entanglement density of the molecular chains, which results in the decrease of the viscosity of the melting HDPE. At the same time, PEG can act as a lubricant in the HDPE mixture, which also could improve the processability of HDPE [21].

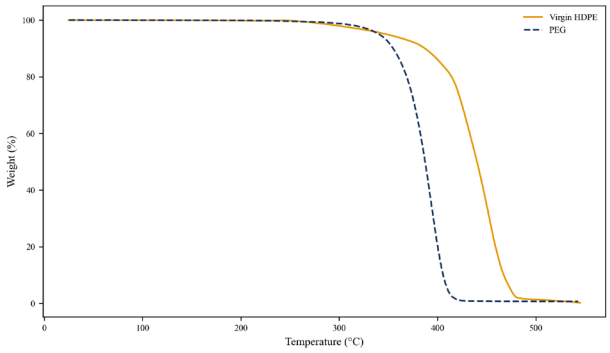

Figure 2.2: TGA of HDPE and PEG to determine maximum temperature zones.

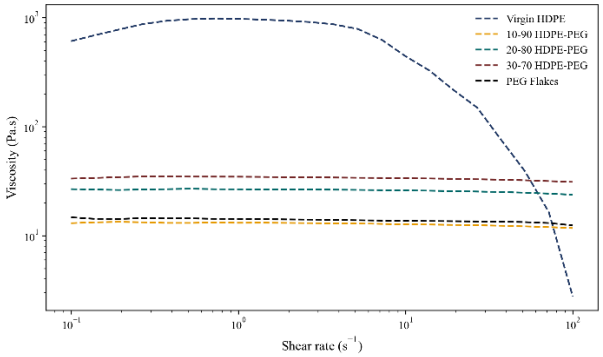

Figure 2.3: Viscosity analysis of HDPE powders and PEG flakes at 175 °C.

These important features based on the viscosity of PEG made it a suitable material to melt blend with HDPE, as well as its water solubility feature to be left with spherical HDPE by itself. HDPE-PEG was washed in a single cycle, and it was noticed that the PEG matrix partially dissolved after 2 hours with applied temperature and constant stirring. The samples were left stirring overnight at the same stirring speed to continuously separate the HDPE particles from the PEG matrix. SEM and FTIR analysis were conducted after the first cycle, and it could be seen that heavy presence of the PEG matrix remained in the HDPE powder. For this reason, a second cycle was conducted at the same applied temperature and magnetic stirring speed to help fully dissolve any remaining PEG matrix that was present within the materials. After the second cycle, SEM and FTIR was conducted on the HDPE powder to validate the effectiveness of multiple rinse cycles to dissolve the PEG matrix. Figure 2.4 shows the FTIR analysis for all mixing ratios, the received HDPE powder was used as a control sample. Samples were tested through a 4 cm^{-1} spectral resolution with 16 scans, and the curves were analyzed using OMINIC software version 8.0. PEG showed peek intensities within 700-1400 cm^{-1}, which are not present in the HDPE powder. After a second rinse cycle, HDPE powder showed no detection of the PEG matrix due to its water solubility feature which ultimately leaves pure HDPE on its own by applying heat and stirring after the second cycle.

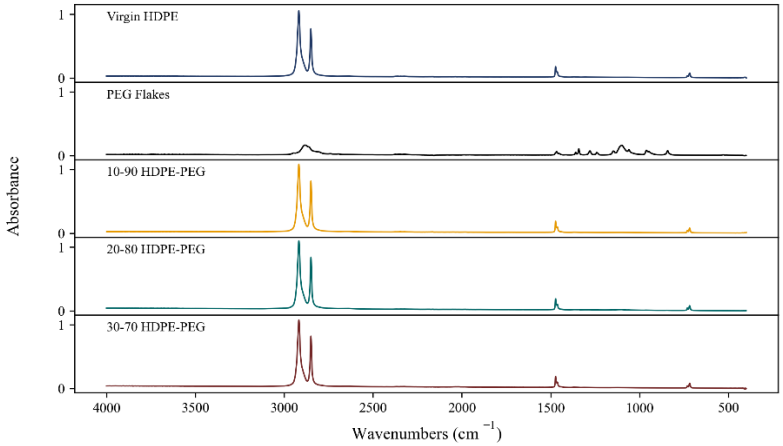

Figure 2.4: FTIR analysis of HDPE, PEG, 10/90 wt. %, 20/80 wt. %, 30/70 wt. %.

2.3.2 Morphology Characterization

During the melt blend extrusion phase for the immiscible materials for the reshaping of the morphology involves the HDPE particles being dragged through the dispersed phase through the hot surface from the mixer walls [22]. Due to the dragging actions that occur within the creation of sheets or ribbons form from the dispersed phase. The sheets or ribbons will become unstable because of the shear and interfacial tension leading to the development of holes within the ribbons that will grow and concentrate until a fragile lace structure forms. The lace structure will then break into irregular-shaped particles which are then broken up into spherical particles. The size and shape of the dispersed phase are controlled by the interfacial tension, rheological properties, and the complex strain field of the mixer [23]. From the interfacial tension created within, the droplets will either revert back into spheres or break up into smaller fragments [14], [15].

SEM images were obtained from as-received HDPE powder, 10/90, 20/80, and 30/70 wt. % mixing ratios to demonstrate the capability of reshaping HDPE morphology. In Figure 2.5, side-by-side comparisons of HDPE shows the creation of spherical particles in comparison to the original irregular shape of HDPE as well as the increase in particle size. Figure 2.5a shows the

irregular shape of HDPE that is seen with all thermoplastic materials. Figure 2.5b shows 10/90 wt. % spherical particles of a mean diameter of 27.57 μm with a good size distribution throughout, which was obtained from the SEM images and using ImageJ software. Figure 2.5c and 2.5d shows spherical particles for 20/80 and 30/70 wt. % with mean diameters of 22.06 and 24.52 μm respectively, as it is seen an increase in particle sizes as the concentration of HDPE increases. To verify the particle size distribution more accurately, an analysis for the particle size for each mixing ratio was examined in comparison to virgin HDPE to see the effects of the final particle size with the increase of HDPE concentration. The values seen in Figure 2.6 show particles sizes of 28.94, 29.59, and 33.54 μm for 10/90, 20/80, and 30/70 wt. % respectfully. The results showed that the average particle size for the fabricated powder decrease from virgin HDPE powder with an average particle size of 58.04 μm, due to the dragging actions within the dispersed phase causing irregular particles to break up into smaller spherical particles. A similar study was conducted previously that showed the capability of increasing a polymers particle size by increasing the concentration respectfully. Shen et al. investigated how to control the particle sizes of poly(methyl methacrylate) (PMMA) by increasing the concentration of the polymer and the increase of the polymerization temperature. The increase in polymerization temperature can cause an increase in the critical chain length due to the increase in solvency of the continuous phase and the increase in the primary material allowed absorption between more oligomer particles to create larger particles [24].

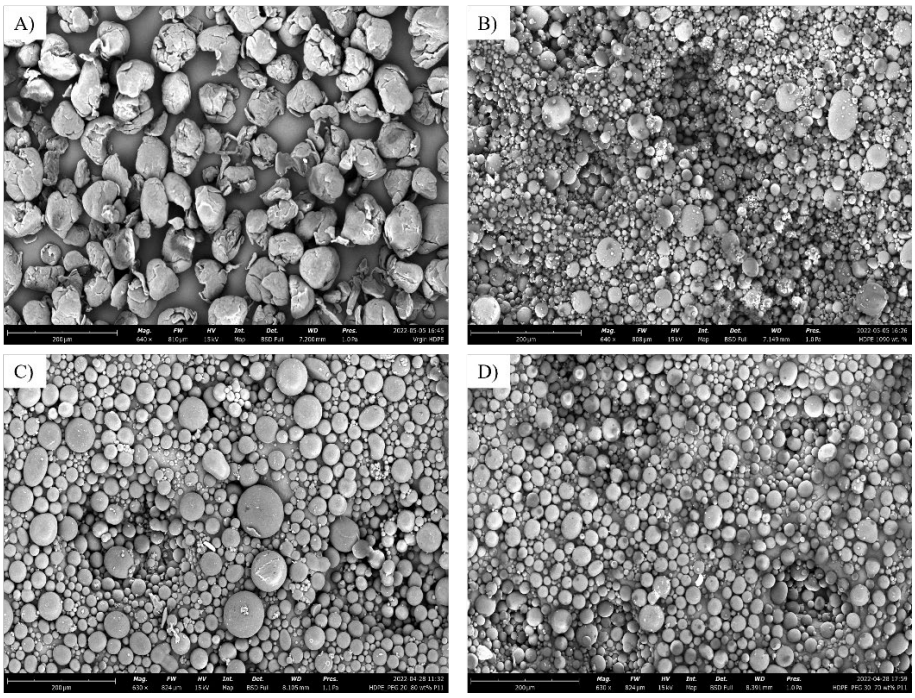

Figure 2.5: SEM images of (a) irregular virgin HDPE, (b) 10/90 wt. % HDPE, (c) 20/80 wt. % HDPE, (d) 30/70 wt. % HDPE.

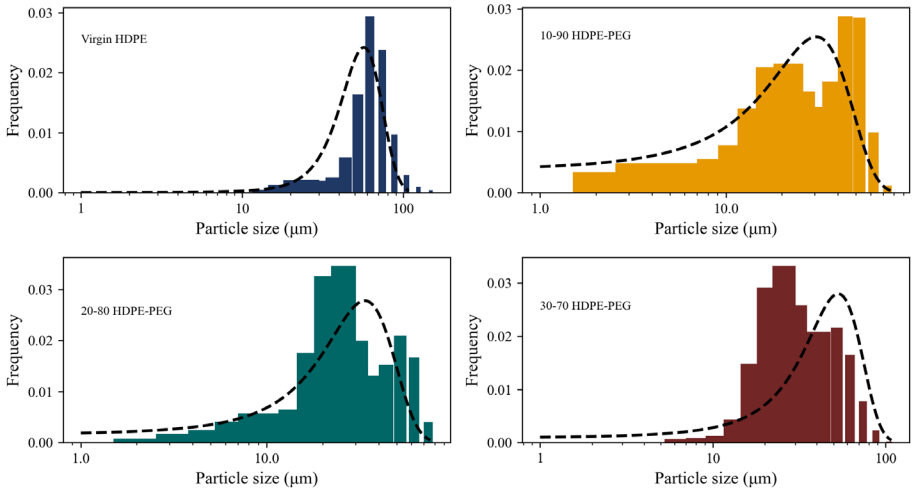

Figure 2.6: Particle size analysis and size distribution (a) Virgin HDPE, (b) 10/90 wt. % HDPE, (c) 20/80 wt. % HDPE, (d) 30/70 wt. % HDPE.

A couple of key features needed to be investigated for the material is the melting temperature (T_m) and re-crystallinity temperature (T_c) which helps determine the sintering window of HDPE. Another key feature was using the area of enthalpy of melting and crystallization temperature to calculate the percentage of crystallinity. To calculate the crystallinity percentage of HDPE, the use of the DSC results was used based on HDPE melting characteristics. The crystallinity (X_c) was used to calculate the ratio of the crystalline part of the semi-crystalline polymer as shown:

$$X_c = \frac{\Delta H_m}{\Delta H_{100}} \times 100$$

where, ΔH_m is the enthalpy which is absorbed by the test sample during the process of heating, ΔH_{100} is the enthalpy absorbed by a sample during the crystallization-melting process which is 293 J/g [25], [26]. Figure 2.7 shows the DSC results of both the crystallinity and melting temperature peaks as well as the area. Table 2.1 shows the data obtained to calculate the crystallinity percentage based on the area of enthalpies for melting and crystallinity. There is a decrease in the crystallinity percentage as it is exposed to thermal treatment. This is caused by time and temperature and powder concentration during the melt blending process [27], [28]. Studies have been conducted to show the effects of temperature on polymer crystallinity. Hoelzel et al. studied HDPE and PP mixtures to study the effects of the melt index of HDPE on the microcellular foaming of HDPE/PP blends, the crystallinity reduction of HDPE, melting temperature, and total amount of crystallinity as a function of the melt index. Neat HDPE with a lower melt index had a higher crystallinity. The crystallinity of HDPE decreased in HDPE/PP blends, regardless of the blend composition and melt index. The total amount of crystallinity also decreased. The crystallinity reduction of HDPE was affected more by the melt index than the crystallinity reduction in the PP fraction [29]. This attributes to HDPE crystallinity percentage decreasing after applied temperature above the melting point and averaging the same percentage for all three mixing ratio values.

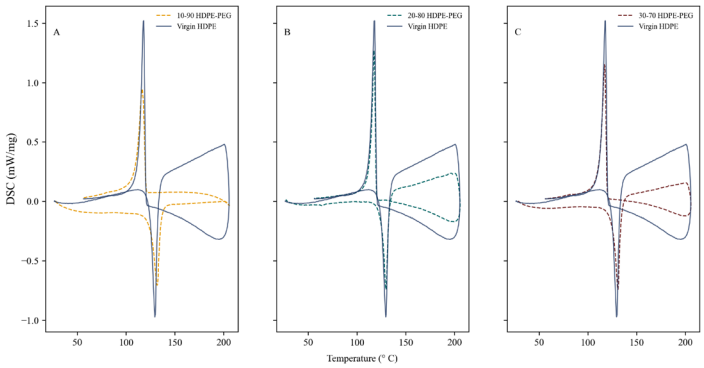

Figure 2.7: DSC analysis in comparison of virgin HDPE to mixing ratios (a) HDPE-10/90 wt. %, (b) HDPE-20/80 wt. %, (c) HDPE-30/70 wt. %.

Table 2.1: Parameters to calculate crystallinity percentage.

	Crystallinity Temperature T_c (ºC)	**Melting Temperature T_m (ºC)**	**Crystallinity Enthalpy Area (J/g)**	**Melting Enthalpy Area (J/g)**	**Crystallinity Percentage (%)**
Virgin HDPE	117.9	129.7	98.23	98.23	77.9
10-90 wt. % HDPE	116.4	132.0	90.55	76.12	56.9
20-80 wt. % HDPE	117.6	129.8	70.31	70.31	54.6
30-70 wt. % HDPE	117	130.9	71.4	71.4	56.8

2.3.3 LS Printability Characterization

The evaluation of packing density was conducted to show the improvement on the reshape of HDPE powder which ultimately contributes to reduce the porosity that occurs with thermoplastics during LS printing [6], [30]. The test was run three times to obtain the standard deviation and normal distribution of the density. Each powder was placed in a graduated cylinder (KIMBLE® KIMAX®) where the volume was calculated of a set height of 10 mL of powder. The total mass was obtained and was then used to calculate the green packing density. Figure 2.8 shows

the results of the packing density, and it showed a higher packing density for 10/90 wt. % of 0.712 g/cm^3 while for 20/80 and 30/70 wt. % the packing density began to linearly decrease to 0.605 and 0.515 g/cm^3 respectively but still shows higher results then the virgin HDPE powder which had a packing density of 0.492 g/cm^3. This is attributed to the increase of spherical particles which occupy more space among the other large particles and effect the arrangement of allowing more particles to occupy the space [31].

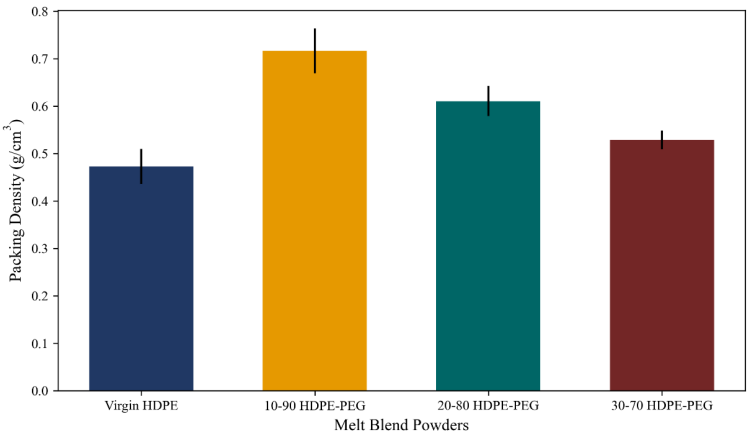

Figure 2.8: Shows the packing density results for each set of powder.

To determine how well the effect of creating spherical and near-spherical particles would influence the printing process a powder flowability test was conducted with all three mixing ratios and compared it to virgin HDPE powder. A total of six trials were conducted for each sample and then the average was obtained to calculate the angle of repose (θ),

$$\theta = tan^{-1}\left(\frac{h}{r}\right)$$

where h is the height of the peak of the powder and r is the radius of the plate underneath the funnel. Table 2.2 shows the results for each powder with the final average and Table 2.3 shows the standard for property chart for powder flowability. Results showed that the virgin HDPE have poor powder flowability with a value of 48.73±1.69 which is a major factor towards thermoplastics

being non LS printable without adding additives [6], [32]. When comparing it to the fabricated HDPE powders it can be observed great improvements in the powders flowability where the powder has good flowability and 20/80 wt. % showing excellent flowability with a value of 26.5 ± 2.35. This is a key feature for LS printing as it allows an almost free flowing behavior that is necessary as LS powders are distributed on the bed for LS machine that uses a roller or blade system and does not self-compact the powder [8]. Flowability also plays a key role in the laser sintering process from the lack of homogeneous and even layers that can lead to porous within and create weak printed parts [33], [34], [35].

Table 2.2: Measurements for each powders flow test trials and angle of repose results.

	Radius (mm)	**Height (mm)**	**Angle of repose (θ)**
Virgin HDPE	24.85	28.39±1.72	48.73±1.69
10-90 HDPE-PEG	50.2	30.25±1.92	31.03±1.59
20-80 HDPE-PEG	22.67	11.32±1.15	26.5±2.35
30-70 HDPE-PEG	21.94	13.87±0.47	31.03±2.39

Table 2.3: Standard flow property chart [36].

Flow property	**Angle of repose (θ)**
Excellent	25-30
Good	31-35
Fair-aid not needed	36-40
Passable-may hang up	41-45
Poor-must agitate, vibrate	46-55
Very poor	56-65
Extremely poor	>66

2.4 Conclusion

This study proposes a methodology to fabricate HDPE spherical particles using MBE for LS application. Different mixture blends of HDPE in a PEG matrix were analyzed; the present

research determined that the HDPE-PEG mixing ratios of 10/90 wt.%, 20/80 wt.%, and 30/70 wt.% produced results with spherical particles with favorable properties for LS printability. Compared to virgin powder, the HDPE fabricated in this study demonstrated spherical morphology. SEM imaging of the spherical HDPE powder showed spherical particles throughout the sample and across all mixing ratios, which demonstrates a successful reshaping of the rough-surfaced, amorphous as-received HDPE. This change in morphology allowed the material to also perform better in properties desired for LS printing, such as increased flowability and packing density, with almost no changes to the sintering window of the material. Particle size distribution was within the range of application for LS, exhibiting a d50 of 24.83 microns for the 20/80 wt.% blend. All mixing ratios showed an improvement in packing density compared to virgin HDPE powder; however, packing density decreased with increasing HDPE concentrations, due to the increasing average particle size. Angle of repose flowability was measured to be 40.4 for virgin HDPE powder. After the MBE process, spherical HDPE powders showed flowability values as low as 26.5 for the 20/80 wt.% HDPE-PEG blend, demonstrating a drastic increase in flowability. These results show enthralling properties for a polymer material destined for LS additive manufacturing. Future work could explore mechanical properties and printing parameters of spherical HDPE powder. Finally, this methodology is applicable for other thermoplastic polymers in the form of powder which exhibit amorphous morphology, and, in turn, poor flowability. Overall, the fabrication of more LS-suitable powder will help alleviate the material bottleneck for this particular AM technology, opening up more possibilities for material applications and properties.

Chapter 3: Laser Sintering of Reshaped High-Density Polyethylene

This chapter investigates the printability of the fabricated reshaped spherical HDPE particle powder for LS printing. Most polymer powders are limited for LS printing due to the particle non-spherical morphology which typically causes prints to fail or have deformations, as well as having large porosity which gives it poor mechanical properties. Therefore, using spherical HDPE powder increases printability for the material and reduces porosity in the printed parts. Printing parameters are established in order to print tensile testing specimens in order to test the materials tensile strengths. Three sets of printing parameters are used with laser power (L_p) being the only parameter to change at 75, 80, and 85%. Printed specimen with L_p of 85% showed the highest strength of 6.42 MPa indicating better melting within the particles improved the parts density giving higher results. XRD analysis are also conducted to view the crystallinity structure as an increase in crystallinity occurs for fabricated spherical particles giving a crystallinity percentage of 80.5% which is higher than standard manufactured HDPE powder which potentially aids in the mechanical properties.

3.1 Introduction

The additive manufacturing (AM) industry has been a growing industry that has allowed the capabilities of rapid production of materials with rapid prototyping, low-cost production, and distributed manufacturing in various fields such as energy departments, aerospace, industrial, and other valued fields of study[1]. In the AM industry, there are seven forms of 3D printing methodologies which include Material Extrusion, Directed Energy Deposition (DED), Binder Jetting, Powder Bed Fusion (PBF) Sheet Lamination, Material Jetting, and Vat Photopolymerization[2]. Selective Laser Sintering (SLS) is a form of PBF which is the application of a powder bed that acts as a self-support system, standard for use of printing polymer powder

materials with complex geometric shape designs[3]. LS forms 3D objects by laser energy to selectively heat powder particles which results in fusion, the fused particles subsequently solidify to form a 3D structure[37]. The main advantages of LS printing is the high resolution and excellent quality with support-free technique due to the support provided by the unbounded powder present around the fabrication [38]–[40]. Some disadvantages of LS printing includes the limitation in powder reliability, the complex merging behavior, and the molecular diffusion process during the process which limits the choice of polymers used in the process[41]. Particle morphology plays a major role in the sintering process and must be a balance between size range and shape of the powder particles [42].

Thermoplastics are a large material class that make it a suitable polymer due to their properties of high thermal stability and resistant to aggressive chemicals such as alkaline solutions, acids, and solvents [43]. Their corrosion resistance, low density, high strength, user friendly design, and recyclability benefit [44] has made it a desirable material in various applications such as aerospace [45] and automotive [46] industries. Various type of thermoplastic materials include polyethylene (PE), polypropylene (PP), polyvinyl chloride (PVC), and polystyrene (PS) [47]. High-density polyethylene (HDPE) is used widely in harsh environments in applications as tubing for drainages and catheters due to its excellent toughness and resistance to fats and oils [48]. The challenge in using HDPE and other thermoplastics for LS printing, is the poor printability and mechanical strengths caused by the non-spherical particles that cause poor powder flowability and high porosity within the prints [49]. Material more suitable for LS printing focus on using spherical shaped particles in the morphonology to make thermoplastics and polymers applicable for printing [50].

Different investigations have been conducted to analyze the benefits of spherical particles with a controlled size range on the overall printability and mechanical strength. Kleijnen et al. fabricated spherical polybutylene terephthalate (PBT) powder through melt extrusion for laser sintering printing and analyzed the printability of the powder and mechanical strength [5]. Yu et al. printed polyamide 12 (PA12) to compare spherical particle PA12 powder with SiC/PA12 which

had better mechanical strength and surface finish in comparison to the PA12 matrix [51]. Song et al. fabricated spherical polyvinylidene fluoride (PVDF)/barium titanate ($BaTiO_3$) for SLS printing through shear milling and plasma technology to investigate the proof-of-concept of spherical powder for LS improved the mechanical properties as well as piezoelectric properties [52]. These investigations show the advantages of using spherical particle powder for SLS printing that improves the powders printability and mechanical strengths.

This work presents the development of optimal printing parameters for fabricated spherical HDPE particle powder for LS printing. Three different sets of prints were printed with different parameters to analyze the tensile strength and understand the influence of spherical morphology allowing the semi-crystalline powder to be LS applicable. SEM images were used to observe the particle adhesion of the powder. Also, DSC and XRD tests were conducted to calculate and measure the crystallinity of HDPE to determine the relation of high mechanical strengths with higher crystallinity. The improvement in powder flowability and packing density of spherical HDPE powder was investigated and how these particle properties impacted the printability features and reduced the porousness inside the printed structure making the powder LS suitable were also the focus of this research.

3.2 Experimental details

3.2.1 Materials

High-Density Polyethylene (HDPE) (AXALTA Coathylene® Fine Powders; average particle size 40-60 μm; density of 0.951 g/cm^3) powder was used as the primary thermoplastic material for the fabrication of spherical particles.

3.2.2 LS Printing

Laser sintering experiments were conducted on a SHAREBOT SNOWWHITE^2 (SHAREBOT S.R.L., Nibionno) that is equipped with a 14 W CO_2 laser with an operating

wavelength of 10.6 μm. The process parameters are listed below in Table 3.1 with laser power being the primary parameter that was changed. The parameters are controlled using Slic3r where the designed model is sliced and the printing parameters are preset prior to uploading the G—code onto the printer system.

Table 3.1: Laser sintering parameters.

	Specimen 1	**Specimen 2**	**Specimen 3**
Laser power (L_p)	75%	80%	85%
Laser scan speed (v_s)	35000 m/s	35000 m/s	35000 m/s
Powder bed temperature (T_{bed})	106ºC	106ºC	106ºC
Layer height (L_h)	0.50 mm	0.50 mm	0.50 mm

3.2.3 Material Characterization

To establish the printing parameters, a differential scanning calorimeter (DSC) test was conducted to determine the sintering window using a DSC 404 F1 Pegasus (NETZSCH). Samples were heated from room temperature to 200 ºC with a heating rate of 5 ºC/min and cooled down at the same rate. To analyze the semi-crystallinity structure between non-spherical, spherical, and LS printed HDPE powder, an x-ray diffraction (XRD) was conducted using a CuKα radiation on a discover diffractometer (Bruker, Boston, MA). Mechanical strengths were tested on all three sets of specimens through tensile strength tests using a ADMET (ADMET, INC., Norwood, MA, USA). Scanning electron microscopy (SEM) imaging was performed to analyze the HDPE porous surface structure using the IT 500 LV Scanning Electron Microscope (JEOL USA, Inc., Pleasanton, CA, USA).

3.3 Results and Discussions

3.3.1 Differential Scanning Calorimeter

DSC tests were performed to determine the peak temperatures of crystallization (T_c) and melting (T_m) which is required for calculating the sintering window for LS printing. The sintering window is the meta-stable thermodynamic region of undercooled polymer melt during LS processing for a given polymer [50]. Figure 3.1 shows a T_m of 129.8 ºC and T_c of 117.6 ºC which gives a sintering window of 12.2 °C. The sintering window is a meta-stable thermodynamic region of undercooled polymer melt for laser sintering processing for any given polymer and for semi-crystalline polymers implies that the crystallization temperature (T_c) should be inhibited during processing and be controlled within the melting temperature (T_m) and T_c [53]. The area of enthalpy for both curves show a melting enthalpy of 107 J/g and a crystallinity enthalpy of 128.8 J/g. The crystallinity (X_c) was used to calculate the ratio of the crystalline part of the semi-crystalline polymer as shown:

$$X_c = \frac{\Delta H_m}{\Delta H_{100}} \times 100$$

Where, ΔH_m , is the enthalpy that was absorbed by the sample during the heating and cooling process and ΔH_{100} is the enthalpy absorbed by a sample during the crystallization-melting process which is 293 J/g [25], [26]. The crystallinity percentage was calculated to be at 80.5%. Crystallization improves the strength and modulus of polymers by reducing the degree of molecular randomization and by orienting the semi-crystalline chains improves the strength and modulus in the orientation direction thus improving the intermolecular bonding and influencing the mechanical strengths [54]. Table 3.2 shows the overall data obtained required to calculate the crystallinity percentage and sintering window.

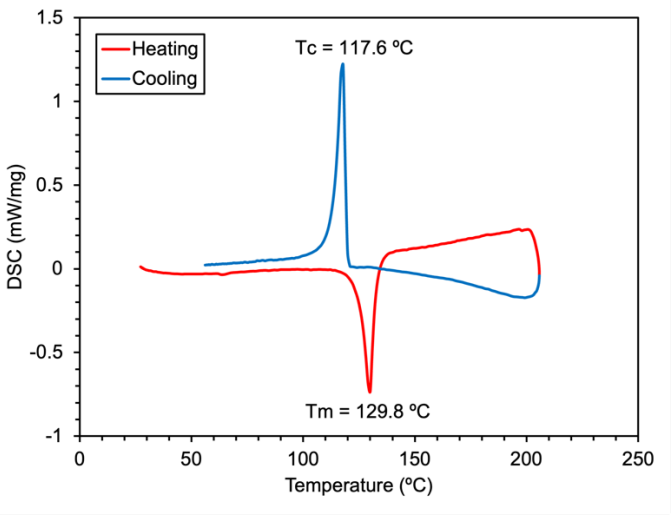

Figure 3.1: DSC analysis of HDPE spherical particles powder sintering window.

Table 3.2: Sintering Window and Crystallinity Percentage Parameters.

	Temperature T_c (°C)	**Temperature T_m (°C)**	**Enthalpy Area (J/g)**	**Enthalpy Area (J/g)**	**Percentage (%)**	**Sintering Window (°C) ($\Delta T = (T_m - T_c)$)**
Spherical HDPE Powder	117.6	129.8	128.8	107	80.5	12.2

3.3.2 Printing Optimization

Multiple laser sintering trials were carried out to test the fabricated HDPE powder with the SnowWhite LS printer until the optimal parameters for a single-layer print were established in Table 1. Powder flowability showed an improvement in the packing density which were attributed to HDPE particles being spherical and with a size range allowing smaller particles to fill voids as the laser melted the powder. Figure 3.2 shows printed specimens demonstrating the printability of HDPE powder with a spherical morphology with full melting of the powder allowing the parts to print with no deformation or complications.

Figure 3.2: LS printed HDPE single-layer tensile specimens. Specimen 1 (A), Specimen 2 (B), and Specimen 3 (C).

3.3.3 X-Ray Diffraction

XRD tests were conducted on HDPE powder that was as received, as fabricated spherical particles, and as LS printed HDPE to compare the crystallinity structure of the powder. The primary characteristic peaks for HDPE are at 21.3°, 23.9°, and 36.6° diffraction angles that are specific for polyethylene characterization with lattice planes (110), (200), and (020) respectively [55], [56] and shows a orthorhombic structure [57]. XRD was also used to validate the increase in mechanical strengths due to the increase of crystallinity percentage. Figure 3.3 shows the three samples crystallinity structure dependent on thermal treatment on the powder. It can be seen that the microstructure found at the surface of the samples presents a higher degree of crystallinity due to the shear and rapid cooling, as well as the enthalpy of fusion considers the defects and voids found in the microstructure causing the values to be lower [58], [59] based on XRD results.

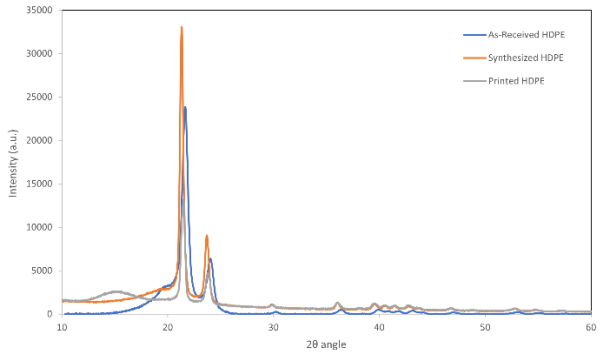

Figure 3.3: XRD analysis of HDPE powder as received, as thermally treated spherical particles, and as LS printed.

3.3.4 Single-Layer Tensile Strength

Five printed HDPE prints per printed specimen with different L_p were tested using ASTM standard D638 to obtain the average tensile strength of single layer printed tensile specimens. The ramp rate was set to 1 mm/min during testing to ensure that the machine grips would maintain grip with the clamps. Figure 3.4(A) shows a printed HDPE tensile design based on ASTM C1557 geometric design in the secured position for tensile strength testing. Strength analysis showed that specimen 3 had the greatest strength with a stress-strain value of 6.42 and 0.005 MPa respectively. This is attributed to the higher density from the adhesion melting with higher laser power and minimal porosity [60], [61]. Specimen 2 had a stress-strain value of 5.56 and 0.015 MPa and specimen 1 had values of 5.17 and 0.12 MPa results respectively. Table 3.3 summarizes the final value results of the strength analysis and Figure 3.4(B) shows plotted graph of the tensile strength results.

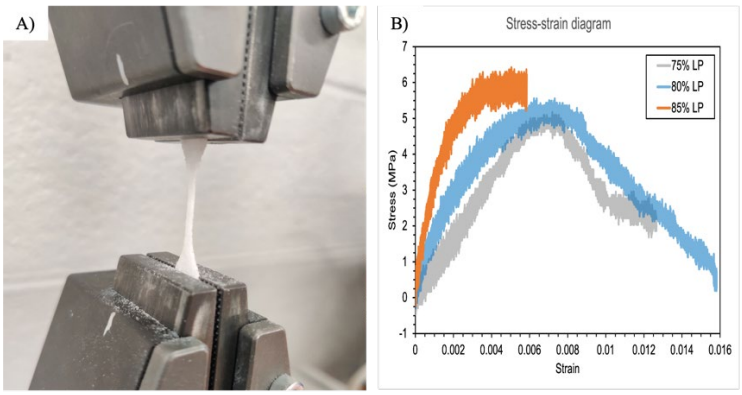

Figure 3.4: HDPE sample in tensile frame loader (A) and HDPE stress-strain results (B).

Table 3.3: Average maximum tensile stress-strain results for LS printed specimens.

	Specimen 1	**Specimen 2**	**Specimen 3**
Stress (MPa)	5.17	5.56	6.42
Strain (m/m)	0.012	0.015	0.006

3.3.5 Scanning Electron Microscopy

SEM images were taken of the cross-sectional area for each specimen to examine the adhesion of the prints and examine the porosity within the printed structure. Figure 3.5 shows spherical particles on the surface edges as particles melted on the outer surfaces. Images show proper melting within the material with little to nonporous in the printed part with porous size smaller than 20 μm for all three different parameter prints. This is attributed to the spherical shape of the particles that allow better flowability more easily and pack more densely than irregular shapes allowing better adhesion [62]. An increase in the layer density can be seen with the increase in laser power. Figure 3.5(C) with a L_p of 85% had greater layer adhesion as it prevented rapid crystallization during the cooling process within the particles from the high temperature within the powder layer to suppress crystallization [63]. All three set parameters allowed for a full melt with

each print yet, the higher L_p gave a greater melt during the printing process allowing the production of a stronger part with the reduction of porosity, as the molten HDPE infiltrates into the voids between the powder spherical particles having a greater density [64].

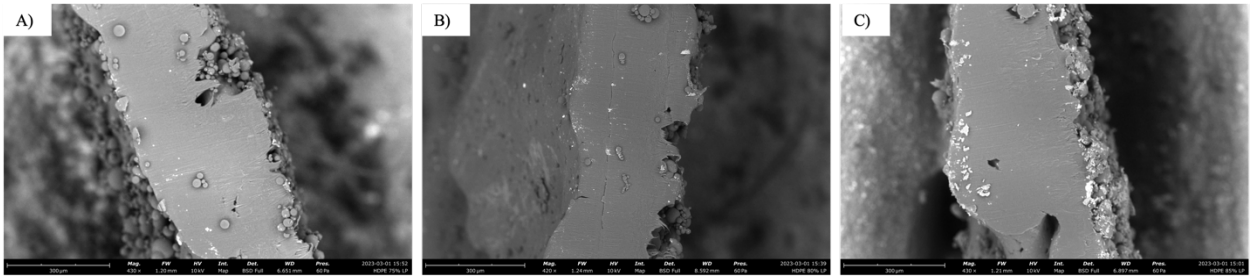

Figure 3.5: Images of cross-section of Specimen 1 (A), Specimen 2 (B), Specimen 3 (C).

3.4 Conclusion

In this study, fabricated HDPE spherical particle powder was used as the printing material for an LS with established printing parameters. Implementing LS additive manufacturing allowed the capability of printing of three different types of tensile test specimens with the LS laser power of 75, 80, and 85%. Additional parameters included a laser scan speed of 35000 m/s, a powder bed temperature of 106 °C, and layer height of 0.50 mm for the printed material. Experimental results show an effective powder melting adhesion within the particles due to the powders improved flowability and packing density from the sphericalness features. SEM images showed little to nonporous within the cross-sectional area from the printed specimens after printing and tensile testing. Porosity was measured with sizes of 20 μm or less in sizes due to the controlled particle size range between 20-80 μm which is the desired range for LS printing. XRD analysis showed an increase of crystallinity from the fabricated HDPE powder in comparison to the printed and as-received powder due to the thermal exposure when fabricated and heat treatment post-process prior

to printing. The XRD results showed the increase in 2θ of 21.3° in the lattice plane of (110) within the orthorhombic structure. The DSC analysis was used to calculate the crystallinity percentage of 80.5% which was slightly higher than standard HDPE material. DSC also was used to determine the sintering window of HDPE powder which was calculated at 12.2°C based on the crystallinity and melting temperature peaks of 117.6 °C and 129.8 °C respectively. Tensile strength tests showed that specimen 3 had a stress-strain value of 6.42 MPa and 0.006 respectively. This was attributed to the small porous printed samples had that helped increase the material's strength. Furthermore, the increase of crystallinity percentage increased the intermolecular bonding within the structure and improved the materials mechanical strength. With the implementation of fabricated spherical HDPE particle powder, LS printed specimens showed better printing abilities and improvement in mechanical strengths. This was attributed to the reduction of porosity within the inner structure of the prints making this semi-crystalline thermoplastic material excellent for LS printing and usage.

Chapter 4: Direct Ink Write Printing of Ceramic Clay with Embedded Wireless Temperature and Relative Humidity Sensor

Clay material is becoming of high interest due to its high corrosion resistance and high temperature resistance while being environmentally friendly and 100% reusable. Implementing it through additive manufacturing is investigated in order to establish ethe proper water-clay (w/c) mixing ratio to obtain a proper viscosity to make the slurry DIW printable with proper flowability and able to maintain its printed shape with minimal cracking during drying process. It is established that 16.2 water wt. % gives the desired viscosity for printing various shapes including a wireless temperature and relative humidity (RH) sensor. Embedded sensor is able to sense at a maximum distance range of 141.7 m with temperatures of 85°F and RH of 65%. Post-process was also conducted to compare fired and non-fired clay samples and test the mechanical strengths. XRD is used to view the clay crystallinity to compare both fired and non-fired samples. This research demonstrates the feasibility of using DIW printing porcelain 5 clay for embedded sensing applications with functional sensing capabilities.

4.1 Introduction

Additive Manufacturing (AM), also known as 3D printing is a manufacturing technique that consists of a layer-by-layer deposition of materials to form a three-dimensional part from a CAD design. AM offers many advantages over traditional manufacturing, due to its easier fabrication process, material availability, and relatively low manufacturing cost, making it a great tool for rapid prototyping of complex geometrical designs. Although many advances have been done for metallic and polymeric materials for AM technology, there is still limited advances in the manufacturing of ceramics. The fabrication of ceramics by AM technology is an area of interest due to their excellent mechanical properties and thermal stability [65]. Most common AM methods

to fabricate ceramics include Direct Ink Write (DIW) [66], Selective Laser Sintering (SLS) [67], Stereolithography (SLA) [68], Binder Jetting (BJ) [69], and Material Jetting (MJ) [70]. Printing techniques such as SLS and BJ allows the fabrication of highly complex geometrical shapes for ceramics. However, the printed parts usually result as low density and poor mechanical properties [71]. On the other hand, printing methods such as SLA and MJ offer the possibility to fabricate high-density ceramics. Nonetheless, SLA and MJ results in a low material selectivity, restricting the fabrication process [72].

DIW is a material extrusion technique that consists of a layer-by-layer deposition of a paste through a nozzle by a pressure driven mechanism onto a substrate. DIW offers a low cost, a relatively fast printing process, and a large selection of printable materials with wide molecular weights, which can be easily controlled by its rheological properties, making it suitable for prototyping. In addition, DIW of ceramics usually does not require a heating temperature or photopolymerization process to retain its structural shape since the shear-thinning properties allows it to self-support during the printing process. The main drawback of using DIW to fabricate ceramics is that usually a post-treatment process is required to fully solidify the printed part. This post-treatment process (i.e., sintering, firing) allows for removal of polymeric binders and moisture while enhancing grain growth of ceramics, which contributes to increase its final density. However, this post-treatment process could also lead to different quality defects including, excessive shrinkage, voids, cracks, and warping [73]. Despite that, the biggest advantage of using DIW technique to fabricate ceramics is that the final parts usually resulted on high-density samples with tunable mechanical properties [74], [75].

Clay is one of the most widely available ceramics. Clays typically consist of a mixture of hydrated aluminosilicates with different ratios of silicon dioxide (SiO_2) and aluminum oxide (Al_2O_3) [66]. Many research studies in clay printing have been used for decorative architectural [76], bioengineering [77], and construction [78] purposes. However, there is very limited information of clay printing applied for embedded sensors. Among different types of clays, porcelain is of particular interest due to its mixture complexity (i.e., clay, kaolin, quartz, and

fluxing agents) and phase transformation during the sintering process that leads to increase its tangent loss at higher temperatures [79]. In addition, the rheological properties of porcelain can be easily controlled by mixing with water, and thus organic additives are not needed, which facilitates the firing process as debinding is not required [79].

Embedded sensors through additive manufacturing has grown over the years with the application of embedding sensing technology directly into manufactured parts in means of protecting sensors from harsh environments as well as prolong the lifetimes of sensors use [80]. One main limitation and challenge with additive manufacturing of embedded sensors field is the ability to create proper structures to fully enclose the sensor and maintain the integrity of structure design [81]. The advantages of implementing embedded sensors withy additive manufacturing allows the freedom of fabricating outstanding geometrical designs with the minimization of tooling for sensor enclosures [82]. Liu et al. investigated various forms of 3D printing flexible strain sensors and testing the sensing mechanisms to view the feasibility of this method [83].

This work presents the development of a paste suitable for DIW printing using Cone 5 Porcelain Clay and deionized water. To demonstrate the printing capabilities of Cone 5 Porcelain Clay, different geometrical samples were fabricated and fired without producing cracks across the surface. In addition, the main purpose of this paste was to be able to embed a sensor during the printing process. The results obtained showed that is possible to fabricate embedded sensors capable to measure temperature and relative humidity through wireless reading, proving the capability of using DIW printing for this application.

4.2 Experimental details

4.2.1 Materials and Fabrication

Cone 5 Porcelain (Armadillo Clay & Supplies, Austin, TX) was selected as a solid loaded clay material (Relative density: ~2.6 gm/cc; Melting point: >1200°C) and deionized (DI) water was used as a solvent for the slurry fabrication. A commercial S2 smart temperature and humidity

sensor (MOAT® TECHNOLOGIES LLC, San Diego, CA) was used to measure thermal and RH readings.

The slurry was fabricated by mixing porcelain clay with DI water to control the viscosity and allow better flowability, printability, and shape retention. Clay slurry was hydrated to be viscous enough to flow through the feeding hose without clogging it, while being capable of retaining its shape after deposition.

4.2.2 Printing and Post-Processing

Clay samples were printed using a Delta WASP Delta 2040 Clay printer (PicoSolutions Group Inc, Kearny, NJ). Samples were printed using a nozzle diameter of 3 mm, print speed of 25 mm/s, layer height of 0.5 mm, and infill set to 30%. Compression disks were printed with dimensions of a diameter of 25 mm with a height of 3 mm. The sensor enclosure dimensions were 41×41x13 mm as seen in Figure 1a and non-fired parts dimensions were 40x40x12 mm as seen in Figure 1b. Printed bisque parts were fired using a KILNMASTER LT (Skutt Ceramics Production Inc., Portland, OR) at 1222.2°C for six hours and then cooled down to room temperature. Figure 4.1 shows porcelain clay samples, a clay non-fired sample (a) and fired sample with applied Cone 6 Glaze (1184-1222°C) (b).

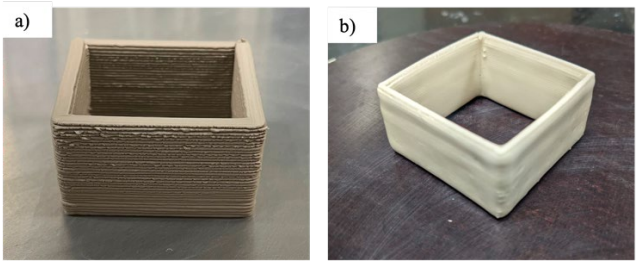

Figure 4.1: Porcelain 5 print through DIW non-fired (a) and fired sample (b).

4.2.3 Printing and Post-Processing

Rotational rheological measurements for the clay slurry were conducted using a DHR-2 rheometer (TA Instruments, New Castle, DE) with a parallel plate geometry. The test was performed with a 0.7 mm gap between the plates at 25°C. The crystal structure was analyzed for non-fired and fired parts by using x-ray diffraction (XRD) using CuKα radiation on a discover diffractometer (Bruker, Boston, MA). The compression test was analyzed for the non-fired and fired parts by using a Instron 60TM-50 (Instron, Norwood, MA) with a 50 kN force capacity.

4.3 Results and Discussions

4.3.1 Rheological Measurements

The viscoelastic properties of the clay slurry is a crucial stage in order to control its shape retention and printability [84]. Universal parameters for creation of slurries does not exist as many variables affect the ceramic's rheological behavior. An important factor in the creation of a slurry is the type of additive selected in the composition of the slurry, such as polyvinyl alcohol, polyethylene glycol and DI water which are commonly used in the fabrication of ceramics using DIW [17], [18]. Incorporating these types of additives allows for the material to flow better, with either Newtonian or Non-Newtonian flow behavior. When the stress is increased to a certain level, non-Newtonian fluids show signs of shear-thinning behavior, such that their viscosity declines significantly as the shear rate rises [19]. Shear thinning behavior is important to be able to extrude the clay without clogging the nozzle and subsequently achieving structural integrity after depositing the extrudate.

This behavior for non-Newtonian fluids (shear-thinning) can also be described by the Herschel-Bulkley model [20]: $\tau = \tau_\gamma + K(\tau)\dot{\gamma}^n$. High solid loading content is also the most preferable parameter while designing a ceramic slurry. Increasing the solid loadings will not only reduce the shrinkage in the final part but high density can also be achieved. Nevertheless, high contents of solid loadings drastically increase viscosity. Rheological data showed when clay was

combined with water at specific wt. % the paste achieved ideal printing viscosity for DIW of between $10^3$and 10^5 Pa^*s [21]. Rheological data was taken for three different clay compositions consisting of 15.0 wt. %, 16.2 wt.%, and 17.4 wt.% (i.e., water to clay) and can be seen in Figure 4.2. The clay slurry with 16.2 wt.% water (approximately 32 vol.% of clay) had optimal shear thinning behavior and achieved a well dispersed slurry with this solid content, having no agglomerations or phase changing during the printing process, resulting in even deposition of layers.

All slurries exhibited non-Newtonian behavior, yet small water percentage changes of ± 1.2 wt.% were shown to significantly influence the viscosity as a function of shear rate. Viscosity increased as the shear rate increased in similar manner in 15.0wt.% compositions and a lower viscosity with 17.4 wt. %, while viscosity for 16.2 wt.% is more stable in decaying linearly with a smaller slope, achieving higher viscosity at higher shear rates, which will not pour beneath particular yield stress [22], [87]. The slurry reached an ideal volume fraction when clay was at 34 vol. % which is the calculated density of the printed part with 16.2 wt. % ratio making it suitable for DIW printing.

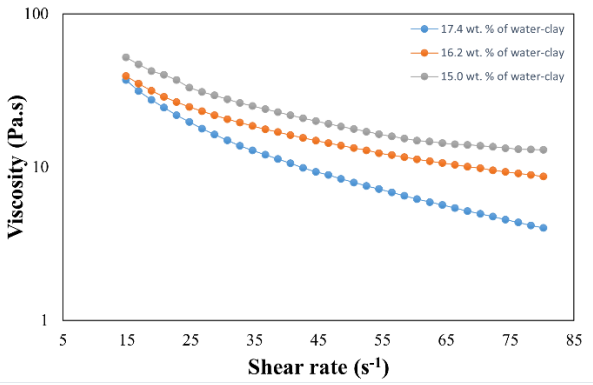

Figure 4.2: Data of viscosity as a function of shear rate for porcelain clay.

4.3.2 Clay 3D Printing Optimization

Printing parameters were established based on the clay slurry viscosity in order to obtain printed parts with different shapes. A nozzle with a diameter size of 1.5 mm was used to maintain a controlled material flow rate. The printing and travel speed was set to 25 and 30 mm/s respectively to allow proper material flowability and reduce material from overflowing of the printed sides. The layer height was set to 0.8 mm and a line width of 1.5 mm to allow proper layer-layer adhesion. Figure 4.3 shows a printed part of a floater cup which demonstrates the results of the materials fabrication and printing parameters. Figure 4.3(A) shows an initial design with minimal support around the handle which caused an overhang to occur and nearly collapse from the weight of the handle base. Figure 4.3(B) was a redesigned model with a shorter and thicker handle with additional supports to prevent overhangs from occurring. Due to the weight of the moisturized clay, the use of more supports was required to retain the printed parts structural design with no failures.

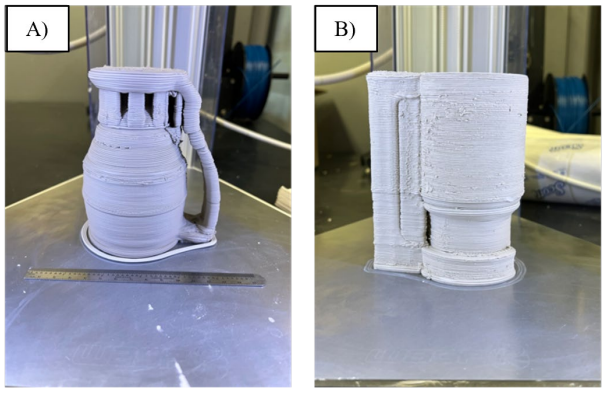

Figure 4.3: Initial (A) and redesigned (B) model design.

4.3.3 Material Fabrication with Embedded Sensor

A customized geometrical design was fabricated to print an enclosure to house a wireless sensor with temperature and RH reading capabilities. The design accounted for the shrinkage

percentage of the clay during the drying process as well as the geometry shape of the sensor. The sensor was fully bounded, and the printed enclosure was left to dry overnight in a room temperature environment. The printed part exhibited minimal caving and deformation on the top surface of the sample and had no cracking during the drying process due to the controlled w/c of 16.2 wt.%. By achieving a proper viscosity of approximately 10^4, the porcelain could maintain its shape while avoiding the top surface from caving in around the edges of the sensor and maintain the intended structural design. The sensor was placed in the center of the printed enclosure mid-print by pausing the printing process and resuming once the sensor was placed as seen in Figure 4.4(A) and Figure 4.4(B).

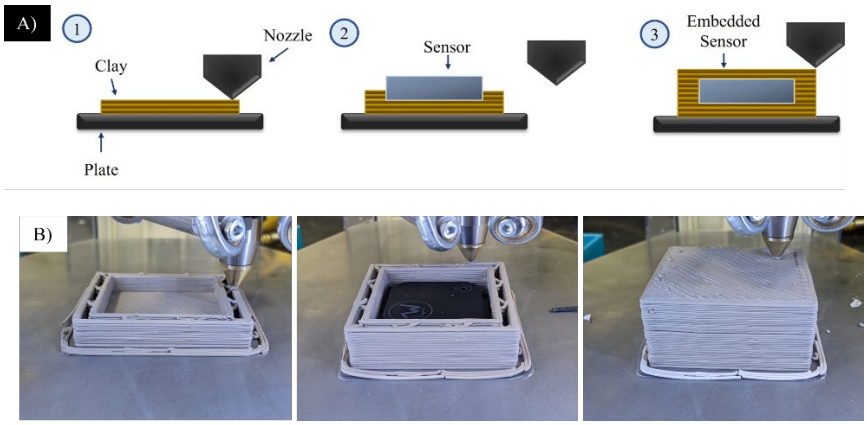

Figure 4.4: Schematic illustration of DIW printing with embedded sensor (A) and images of the embedded sensor printing stages (B).

4.3.4 X-Ray Diffraction Analysis

In Figure 4.5, the Porcelain 5 phase analysis is shown through XRD analysis. A comparison between non-fired and fired samples were conducted to characterize the crystallinity phases of the samples after high temperature post-processing. Analysis showed a decrease in crystallinity within the fired sample at 2θ at 25º and 27º, which indicates an increase in the glassy phase due to the melting of quartz, while maintaining a constant mullite percentage [88]. Similar results have shown

that an increase in temperature during post-processing of (1300 ºC) leads to a decrease in the peak intensity within the same angle range [89], [90]. Jeoung-Ah showed similar results when running an XRD on paper composite porcelain that were fired at different temperatures to examine the peaks which showed a decrease in the ∝-quartz and mullite structure [91].

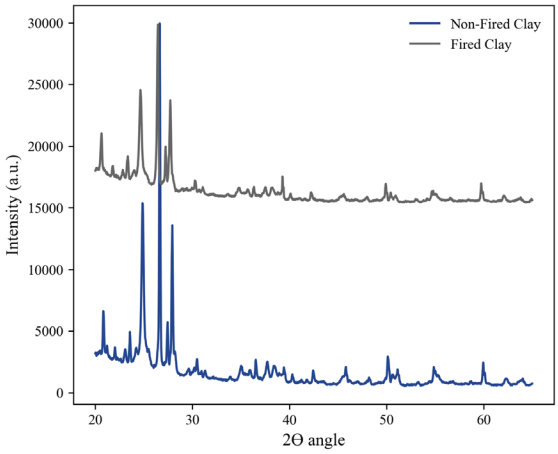

Figure 4.5: Porcelain clay XRD of non-fired and fired clay samples.

4.3.5 Compression Test

Non-fired and fired clay samples were tested under compression. Non-fired clay samples had a higher ultimate strain, demonstrating a more elastic behavior and achieving double strain percentages than fired clay (1.0% vs. 2.0% at 70 MPa) as seen in Figure 4.6. Fired samples were denser due to grain growth during sintering and since the water was evaporated during the heat treatment process. The samples became brittle, therefore reducing their elastic properties [92]. These results are consistent with studies that show that clays that have moisture present or that have regained moisture after firing increase their expansive strain as well as mass gain, mainly arising from water content or rehydration processes [93]. Fired clay undergoes a steeper curve of stress vs. strain relation, having less change in lengths when experimenting the same loads over

the same amounts of time as non-fired clay. Fired clay shows a more rigid behavior with sharp but short increments in strain, opposed to non-fired clay which has a smoother curve with an exponential tendency. The same phenomena can be assumed for non-fired clay in this case study. Fired samples contain higher contents of water and mass after undergone a sintering process that evaporated their water content [94].

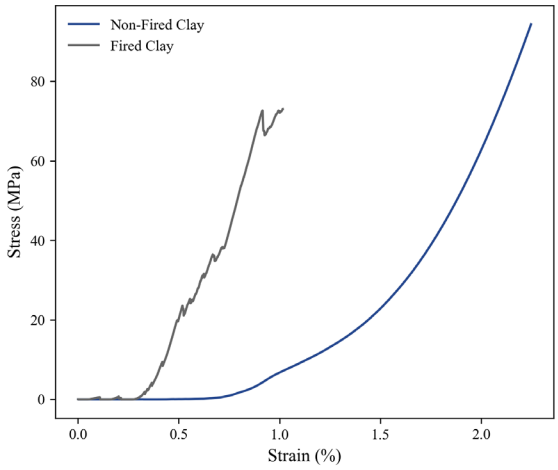

Figure 4.6: Stress vs. strain compression analysis of non-fired clay vs. fired clay.

4.3.6 Temperature and Relative Humidity Sensing

Sensing data at uncontrolled levels of temperature and humidity for the embedded sensor were recorded simultaneously. The “Moat Tech” sensor has a tested range of 121 m and records data every second, nevertheless wireless sensing capabilities of the embedded device were measured at a maximum distance of 141.7 m, meaning the clay enclosure did not have any impact on reducing data transmission distances. Temperature reading showed it was capable of reading the sensors maximum temperature of 85°F and RH of up to 40%. Figure 4.7 shows the temperature and RH readings with respect to time, both measurements were analyzed in concurrently with maximum distance determination.

The embedded sensor was placed under uncontrolled conditions on an outdoor environment for data acquisition to access the capabilities of the embedded sensor reading outdoor environment temperatures. It can be observed that the embedded sensor has a delay of approximately 600 seconds (25 second delay when not embedded) before external conditions penetrate clay enclosure and the sensor can perceive the environmental conditions. RH and temperature are correlated and shown the same peaks and downshifts during the same periods of time, most noticeable at 900 seconds and 1,000 seconds.

The clay enclosure provides the sensor with protection for harsh environments, allowing constant monitoring. While the thick porcelain barrier has low transmissivity of environmental conditions, it only translates to a delay of 10 minutes (600 seconds) of data capturing which outweighs the time and resources needed to take periodic measurements of typical harsh environments such as the case of nuclear waste storage, which requires periodic monitoring of tanks using Type B – Platinum rhodium 30% Rh-Platinum rhodium 6% Rh thermocouples which allow measurements up to 1700°C, very stable thermocouple but less sensitive in the lower range, along with capacitive sensors to take relative humidity data, while these last ones can last for long transient periods, they are characterized for their large variations **[95]**. The sensor had capabilities to transmit data within the enclosure of the clay housing without disrupting the signal's accuracy as it was within normal operating conditions, ±0.3°C/±0.5°C for temperature and ±3.0% for RH, comparable to similar temperature sensors operating under ceramic enclosures **[96]**.

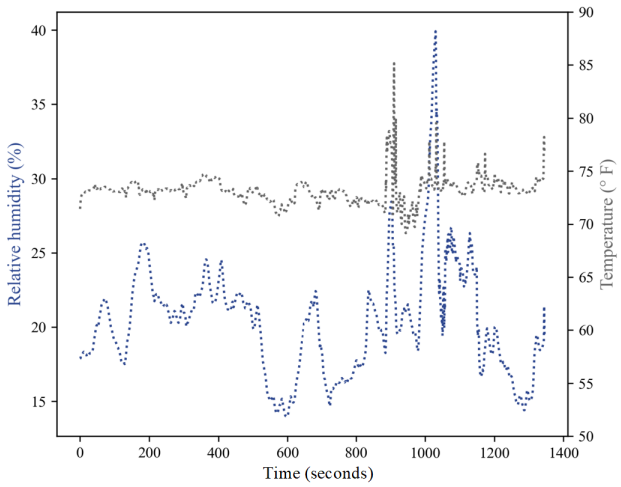

Figure 4.7: Relative humidity and temperature readings over time from the clay embedded sensor measured at 141.7 m.

4.4 Conclusion

In this study, Cone 5 porcelain clay was fabricated with an embedded wireless temperature and relative humidity sensor through DIW printing. Implementing DIW printing allowed the capabilities of freedom of design in printing structures for the enclosure of the sensing unit. With the established printing parameters with a printing speed of 25 mm/s, layer height of 0.5 mm, infill density of 30% and using a nozzle diameter of 3 mm allowed the printing of the material with proper flowability for proper layer-layer printing. This showed effective with the printed designs that aided in avoiding structural deformation and minimal overhang from layer-layer of the prints. The optimal water-clay mixing ratio of 1:5 allowed proper printing process with good flowability of the porcelain clay while still allowing the parts to maintain shape retention and minimal shrinkage to avoid cracking during the drying. The compression strengths from fired and non-fired samples were studied, showing strengths of 70 MPa for the fired sample and 90 MPa for non-fired. An investigation in the crystallinity phase showed a small decrease within the mullite after applied temperature during the firing process which caused melting in the quartz causing an increase in the glassy phase. The embedded sensor showed the capability of gathering readings while being

enclosed within the clay at distances within 141.7 m from the reader. With clays particles, it allowed the increase in the electromagnetic on the surface of the material which allowed the frequency of the sensor to be able to be obtained for thermal analysis. Results of sensing show temperature readings of 85 °F with humidity sensing of up to 40% continuously while embedded within the printed enclosure while being in an outdoor uncontrolled environment. The feasibility of this application allows the usage as self-storage containers for hazardous materials or be used in harsh environments without sacrificing the signal strength of the sensor within the enclosure. With Cone 5 Porcelain corrosion resistance properties and great heat capacity makes it a suitable insulating enclosure for these applications and usage.

Chapter 5: Fabrication of Multilayered Copper and Zirconium Silicate for Embedded UHF RFID Temperature and Relative Humidity Sensing by Multi-Material Printing

Multi-material printing is an innovative method through AM that allows the capability of printing multiple materials on the same deign. The use of FFF 3D printing allowed it to be capable to print Cu and $ZrSiO_4$ to make a temperature housing enclosure. Both materials hold similar corrosion resistant and high temperature resistant properties making them ideal for the sensor. The Cu material is used as an outer wall shell for the brittle $ZrSiO_4$ ceramic material in which the wireless sensor is embedded within the ceramic layers. The UHF RFID passive temperature and relative humidity sensor is capable of obtaining thermal readings of temperatures of up to 27 °C and RH of 27% at a maximum range of 0.6 m. The distance range is impacted by the number of layers surrounding the sensor yet demonstrates the ability to still obtain readings. Compression tests are conducted to evaluate the Cu prints, $ZrSiO_4$ prints, and the multi-material prints strengths. This research demonstrates the capability of using FFF multi-material printing Cu and $ZrSiO_4$ to design and fabricate a sensor enclosure with full functionality of temperature and RH sensing capabilities.

5.1 Introduction

Additive manufacturing (AM), normally referred to as 3D printing takes a computer-aided design (CAD) file which is converted to a stereolithography (STL) file and rapid prototyping of the part with desired material [97]. With the improvement of AM technology advantages for these technologies enables and facilitate the production of moderate to mass quantities of products that can be customized individually opening new opportunities in regards to production paradigm and manufacturing capabilities [98]. The AM technology does have limitations and disadvantages such as low production rates, limited materials, and high geometric tolerances [99]. The fabrication of

metals and ceramics is of high interest due to their great corrosion resistance, resistance to aggressive environments, and resistance to high temperatures [100], [101]. Fused filament fabrication (FFF) is an extrusion-based printing technology for feedstock materials and is one of the most widely used forms of 3D printing [102].

The use of FFF 3D printing technology allows the capabilities of printing metallic [103]–[105] and ceramics [106], [107]. Many studies are done with the development and advancement of making metals and ceramics printable using FFF printing. Miclette et al. investigated low-viscosity metal injection molding (MIM) to validate the capacity of AM printer to produce functional components [108]. Gutierrez et al. investigated tensile properties of 17-4PH stainless steel that was fabricated through material extrusion AM and how to improve the strengths of the material [109]. Li et al. tested silicon carbide ceramic substrate in preparation of high precision, high strength, and high density by implementing it through material extrusion and laser cladding and test the materials properties [110]. Hur et al. researched practical methods for ceramic additive manufacturing using sol-gel-based ceramic slurry with polymeric additives to increase the ceramic content in the feedstock [111].

Multi-material printing is a unique form of AM that enables rapid design and direct fabrication of 3D parts consisting of multiple materials without needing complex manufacturing process [112]. This method allows various techniques including embedded sensors applications within the multilayer prints. Nassar et al. manufactured a light emitting diode (LEDs) strain sensor and electronics in multi-material polymer-based print and demonstrated the feasibility for soft packaging of electronic and component sensors [113]. Hainsworth et al. presented an actuator with an integrated print-in-place strain sensor produced with multi-material AM which required no post processing or manual fabrication steps [114]. Shih et al. designed a sensor that can be co-fabricated with soft robotic bodies using muti-material printing without additional modifications and investigated an analytical comparison to sensors [115].

This work presents the implementation of multi-material printing of Cu and $ZrSiO_4$ through FFF printing with an embedded UHF RFID temperature sensor. The demonstration of the printing capabilities of CU-$ZrSiO_4$ with freedom of design allowed the fabrication of a sensor enclosure while embedded within the ceramic $ZrSiO_4$ layers. The results obtained showed the feasibility in this application while being able to obtain temperature and RH sensing analysis through wireless reading, implying the method of using multi-material FFF printing for this application.

5.2 Experimental details

5.2.1 Materials

Copper filament (The Virtual Foundary, Stoughton, WI) was selected as the metal material (Density 4.8 g/cm^2 – 5.0 g/cm^2) for the outer surface shell. Zirconium Silicate ceramic filament (The Virtual Foundary, Stoughton, WI) was selected as the secondary material (Density 2.11 g/cm^2) for the inner shell in which the sensor will be embedded within the layers. A UHF RFID passive sensor (Atlas RFID Solutions Store LLC, Birmingham, AL) was used to measure the temperature and RH readings.

5.2.2 Multi-Material Printing

Both Cu and $ZrSiO_4$ filaments were printed using a Raise3D E2 printer (RAISE3D, Irvine, CA). Filaments were extruded using a 0.6 mm nozzle diameter with printing parameters shown in Table 5.1. The set parameters were used to print compression disks with the set parameter of 12.7 mm diameter and length of 25.4 mm based on ASTM D695 standard. Figure 5.1(A, B) images show multi-material print parts and Figure 5.1(C) shows compression disk printed at a layer height of 0.2 mm as the minimum set parameter for filament layer deposition.

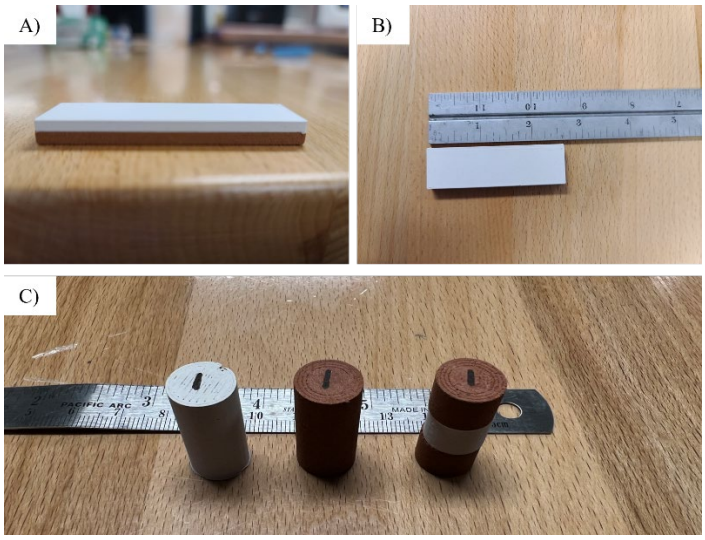

Figure 5.1: Cu-$ZrSiO_4$ print side view (A), top view (B), and compression disks (C).

Table 5.1. Printing parameters for multi-material print and compression disks.

	Printing speed	Nozzle temperature	Bed temperature
Copper	40 m/s	247 ºC	65 ºC
Zirconium Silicate	40 m/s	247 ºC	85 ºC

5.2.3 Material Characterization

Layer adhesion within the printed parts that contained the embedded sensor inside the enclosure was analyzed using a ME520T Amscope microscope (MICROSCOPE CENTRAL, Feasterville, PA). Compression tests were conducted using an Instron 60TM-50 (Instron, Norwood, MA) with a 50 kN force capacity for all three printed samples until failure. Printed materials densities were calculated using a Sartorius YDK03 (Sartorius, Goettingen, Germany).

5.3 Results and Discussions

5.3.1 Density

Printed compression samples densities were evaluated to compare them to the manufactured densities provided. Figure 5.2 shows a graph of the average densities per samples as

Table 5.2 provides the results obtained for each individual sample piece and can be seen a decrease in density after being printed. Cu showed a decrease in density of 12.5% and $ZrSiO_4$ had a decrease of 0.47% respectively. This is attributed to the layer-layer base construction which introduces inherent porosity which is a function of the printing parameters and materials properties, yet is a common defect with FFF printing [116]. The presences of porous within the internal structure is formed during the deposited strands [117]–[119] and the bonding areas between the strands [120].

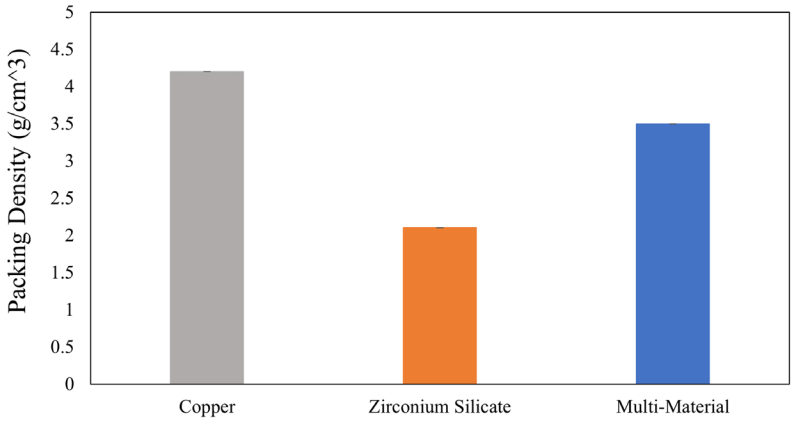

Figure 5.2: Graph of the average densities of manufactured parts.

Table 5.2: Density results for three printed sample materials.

Density (g/cm^3)	Copper	Zirconium Silicate	Multi-material
Sample 1	4.23	2.06	3.42
Sample 2	4.19	2.07	3.52
Sample 3	4.21	2.06	3.50
Sample 4	4.19	2.05	3.52
Sample 5	4.20	2.05	3.31
Average	**4.20**	**2.06**	**3.45**

5.3.2 Multi-Material Fabrication with Embedded Sensor

A customized geometrical design of the sensor enclosure was created using Fusion360 software (Autodesk, USA) and sliced using Ideamaker (version 4.4.0 Alpha) 3D slicer. The set printing parameters allowed for proper filament extrusion and layer-to-layer adhesion between both materials as seen in the schematic illustration in Figure 5.3. The bed temperature was kept at 65 °C for the Cu base layer to avoid melting the Cu material onto the bed and to ensure the first layer stayed intact on the printing bed. The sensor enclosure accounted for the 0.3 mm thickness of the RFID sensor and final printed design had a length, width, thickness of 112.28 mm, 34.8 mm, and 3.19 mm respectively. To embed the sensor during the printing process, the deposition of $ZrSiO_4$ layers was accounted until it reached the design sensor space given at 2.52 mm layer height. As the Cu filament completed extruding the outer walls a 40 s transition occurs between the Cu and $ZrSiO_4$ nozzle as the extruder must reheat to desired nozzle temperature allowing the placement of the sensor in the center surface of the ceramic of the print without pausing the printer. The sensor was placed in the center of the print during the transition of extruders from Cu to $ZrSiO_4$ and placed in the middle of the design. With the set printing parameters and sensor design, the wireless passive sensor was fully enclosed within the multi-material print of Cu-$ZrSiO_4$.

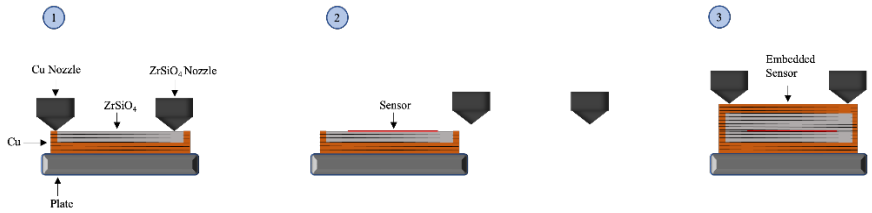

Figure 5.3: Schematic illustration of FFF printing with embedded sensor.

5.3.3 Microscope Images

Microscope images were obtained of the cross-sectional area of the print to view the layer-to-layer adhesion after the embedded sensor was embedded within and are seen in Figure 5.4.

Images show that the layers properly melted on top of each other with no deformation from the sensor. Porosity can be viewed from the cross-section in Figure 5.4(a) and surface Figure 4(b) of the copper finish. This can be attributed to incomplete fusion that occurred during the extrusion process and improper bonding from the layer-layer deposition [121]. Since FFF is a method in which filament is extruded into layer-layer on top of each other potentially leads to formation of porosities and is expected to occur [122], [123].

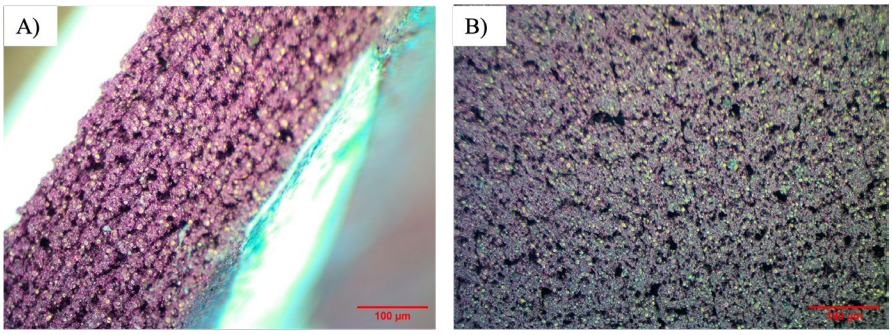

Figure 5.4: Microscope images of cross-sectional area (a) and surface area (b)

5.3.4 Temperature Sensing Analysis

Thermal sensing analysis were conducted to obtain readings of the sensor embedded inside the housing enclosure and results are graphed in Figure 5.5. Analysis showed that the sensor was functional while embedded in the layer-layer of $ZrSiO_4$ material and fully enclosed inside the Cu outer walls. Temperature readings showed a maximum temperature of 82.7ºC and a relative humidity (RH) of 30% at a maximum reading range of 0.6 m. The strength in sensors distance decrease is caused by the number of layer deposition around the sensor to tune the communication performance between the sensor and antenna [124]. Results demonstrate a decrease in RH as temperatures increased indicating proper measurements in that environment. Enclosed sensor readings were compared for accuracy using a temperature and RH meter (Omega Engineering Inc.,

Norwalk, CT). Comparison reading showed an accuracy of the temperature reading of ± 2ºC and RH accuracy reading of ± 1.5%.

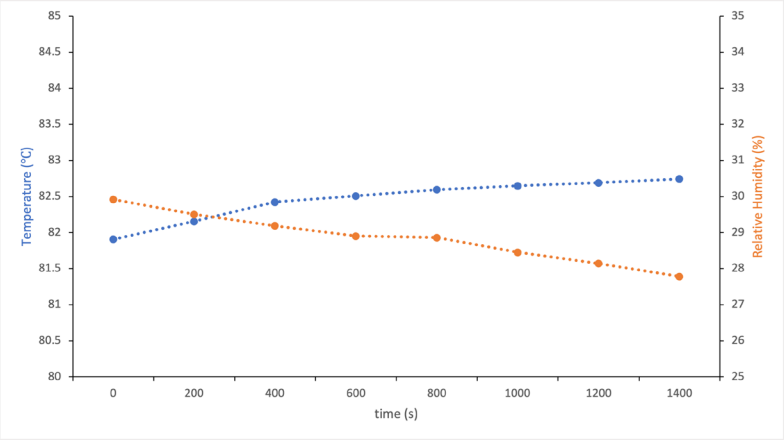

Figure 5.5. Temperature and RH sensing analysis of embedded sensor within multi-material print.

5.3.5 Compression Testing

Compression tests were conducted on pure Cu prints, pure $ZrSiO_4$ prints, and multi-material prints to analyze the differences in stress-strain curves. Five samples were tested per print to obtain the average for each compression analysis Figure 5.6(A) and images of the compressed disks can be seen in Figure 5.6(B). Results showed that $ZrSiO_4$ experienced a maximum compressive strength of 3.5 MPa before fracture. The Cu sample showed a maximum strength of 1.2 MPa and the multi-material print had a maximum strength of 0.7 MPa before fracture. The $ZrSiO_4$ shows different results different from polymers and metals, due to the ceramic characteristics show different plastic deformations as the infill density potentially increased during 3D printing, making cracks occur at different layers showing irregular stress-strain results [125]. The multi-material print showed the lowest compressive strength due to failure from the Cu printed base.

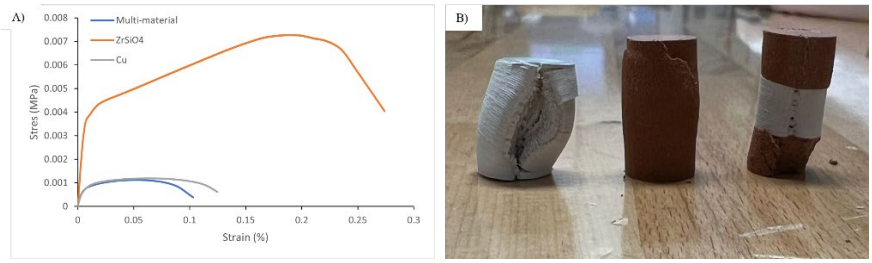

Figure 5.6: Stress-strain compression analysis of printed parts (A) and images of the compression disks (B).

5.4 Conclusion

In this study, multi-material FFF printing was used to embed a wireless UHF RFID passive temperature and RH sensor using Cu and $ZrSiO_4$ as the primary two materials. FFF printing allowed the freedom of design to print the sensor enclosure within the $ZrSiO_4$ layers while the Cu was used as an outer filament shell. Microscopic images of the cross-sectional area demonstrated no deformation and proper layer-layer adhesion during printing keeping structural design integrity. Density analysis showed a decrease in density that is attributed during the printing process. Formation of pores in the layered structures were seen in the images of both surfaces are and cross-section. Compression tests showed $ZrSiO_4$ had a maximum strength of 3.5 MPa before fracture due to initiation of cracks at different layers that demonstrate ceramic irregular stress-strain patterns. Temperature and RH sensing analysis showed thermal analysis of maximum temperature of 82.7 °C and RH of 30% respectively within the layers of the printed sensor enclosure at a maximum sensing distance of 0.6 m. The range of reading between the sensor and reader is caused by the number of printed layers from the two printed materials enclosing the sensor ultimately impacting the sensitivity of the sensor. The application allows the capability of fabricating enclosures that can withstand harsh environments due to the high corrosion and high temperature

resistance of both materials. This allows materials as such to be a suitable source for various of applications in different industry fields that can be implemented with additive manufacturing. With the ability to design and 3D print various sensor enclosures with freedom of design using FFF printing, makes it suitable as the primary method for multi-material printing these two materials for sensors enclosures.

References

[1] K. V. Wong and A. Hernandez, "A Review of Additive Manufacturing," *ISRN Mech. Eng.*, vol. 2012, pp. 1–10, Aug. 2012, doi: 10.5402/2012/208760.

[2] U. M. Dilberoglu, B. Gharehpapagh, U. Yaman, and M. Dolen, "The Role of Additive Manufacturing in the Era of Industry 4.0," *Procedia Manuf.*, vol. 11, pp. 545–554, Jan. 2017, doi: 10.1016/j.promfg.2017.07.148.

[3] J. P. Kruth, X. Wang, T. Laoui, and L. Froyen, "Lasers and materials in selective laser sintering," *Assem. Autom.*, vol. 23, no. 4, pp. 357–371, Jan. 2003, doi: 10.1108/01445150310698652.

[4] A. Mokrane, M. Boutaous, and S. Xin, "Process of selective laser sintering of polymer powders: Modeling, simulation, and validation," *Comptes Rendus Mécanique*, vol. 346, no. 11, pp. 1087–1103, Nov. 2018, doi: 10.1016/j.crme.2018.08.002.

[5] R. G. Kleijnen, M. Schmid, and K. Wegener, "Production and Processing of a Spherical Polybutylene Terephthalate Powder for Laser Sintering," *Appl. Sci.*, vol. 9, no. 7, Art. no. 7, Jan. 2019, doi: 10.3390/app9071308.

[6] J. W. Stansbury and M. J. Idacavage, "3D printing with polymers: Challenges among expanding options and opportunities," *Dent. Mater.*, vol. 32, no. 1, pp. 54–64, Jan. 2016, doi: 10.1016/j.dental.2015.09.018.

[7] A. D. Valino, J. R. C. Dizon, A. H. Espera, Q. Chen, J. Messman, and R. C. Advincula, "Advances in 3D printing of thermoplastic polymer composites and nanocomposites," *Prog. Polym. Sci.*, vol. 98, p. 101162, Nov. 2019, doi: 10.1016/j.progpolymsci.2019.101162.

[8] M. Schmid, A. Amado, and K. Wegener, "Polymer powders for selective laser sintering (SLS)," presented at the PROCEEDINGS OF PPS-30: The 30th International Conference of the Polymer Processing Society – Conference Papers, Cleveland, Ohio, USA, 2015, p. 160009. doi: 10.1063/1.4918516.

[9] W. Zhu, C. Yan, Y. Shi, S. Wen, J. Liu, and Y. Shi, "Investigation into mechanical and microstructural properties of polypropylene manufactured by selective laser sintering in comparison with injection molding counterparts," *Mater. Des.*, vol. 82, pp. 37–45, Oct. 2015, doi: 10.1016/j.matdes.2015.05.043.

[10] S.-J. Wang, J.-Y. Liu, L.-Q. Chu, H. Zou, S.-J. Zhang, and C.-J. Wu, "Preparation of polypropylene microspheres for selective laser sintering via thermal-induced phase separation: Roles of liquid–liquid phase separation and crystallization," *J. Polym. Sci. Part B Polym. Phys.*, vol. 55, no. 4, pp. 320–329, 2017, doi: 10.1002/polb.24275.

[11] Y. Wang, J. Shen, M. Yan, and X. Tian, "Poly ether ether ketone and its composite powder prepared by thermally induced phase separation for high temperature selective laser sintering," *Mater. Des.*, vol. 201, p. 109510, Mar. 2021, doi: 10.1016/j.matdes.2021.109510.

[12] P. Hejmady, "A processing route to spherical polymer particles via controlled droplet retraction," *Powder Technol.*, p. 11, 2021.

[13] H. Ghanbar, C. J. Luo, P. Bakhshi, R. Day, and M. Edirisinghe, "Preparation of porous microsphere-scaffolds by electrohydrodynamic forming and thermally induced phase

separation," *Mater. Sci. Eng. C*, vol. 33, no. 5, pp. 2488–2498, Jul. 2013, doi: 10.1016/j.msec.2012.12.098.
[14] H. Li and U. Sundararaj, "Morphology Development of Polymer Blends in Extruder: The Effects of Compatibilization and Rotation Rate," *Macromol. Chem. Phys.*, vol. 210, no. 10, pp. 852–863, 2009, doi: 10.1002/macp.200800543.
[15] D. Drummer, M. Medina-Hernández, M. Drexler, and K. Wudy, "Polymer Powder Production for Laser Melting Through Immiscible Blends," *Procedia Eng.*, vol. 102, pp. 1918–1925, Jan. 2015, doi: 10.1016/j.proeng.2015.01.332.
[16] X. Yang, Y. Wei, S. Xi, Y. Huang, M. Kong, and G. Li, "Preparation of spherical polymer powders for selective laser sintering from immiscible PA12/PEO blends with high viscosity ratios," *Polymer*, vol. 172, pp. 58–65, May 2019, doi: 10.1016/j.polymer.2019.03.066.
[17] Y. Zhou, S. Xi, Y. Huang, M. Kong, Q. Yang, and G. Li, "Preparation of near-spherical PA12 particles for selective laser sintering via Plateau-Rayleigh instability of molten fibers," *Mater. Des.*, vol. 190, p. 108578, May 2020, doi: 10.1016/j.matdes.2020.108578.
[18] I. Hwang, C.-Y. Kang, and J.-B. Park, "Advances in hot-melt extrusion technology toward pharmaceutical objectives," *J. Pharm. Investig.*, vol. 47, no. 2, pp. 123–132, Mar. 2017, doi: 10.1007/s40005-017-0309-9.
[19] A. S. Abbas and M. G. Saber, "Thermal and Catalytic Degradation Kinetics of High-Density Polyethylene Over NaX Nano-Zeolite," *Iraqi J. Chem. Pet. Eng.*, vol. 17, no. 3, pp. 33–43, Sep. 2016.
[20] M. Xie and H. Li, "Mechanical properties of an ultrahigh-molecular-weight polyethylene/polypropylene blend containing poly(ethylene glycol) additives," *J. Appl. Polym. Sci.*, vol. 108, no. 5, pp. 3148–3153, 2008, doi: 10.1002/app.27919.
[21] Y. Li, H. He, Y. Ma, Y. Geng, and J. Tan, "Rheological and mechanical properties of ultrahigh molecular weight polyethylene/high density polyethylene/polyethylene glycol blends," *Adv. Ind. Eng. Polym. Res.*, vol. 2, no. 1, pp. 51–60, Jan. 2019, doi: 10.1016/j.aiepr.2018.08.004.
[22] C. E. Scott and C. W. Macosko, "Model experiments concerning morphology development during the initial stages of polymer blending," *Polym. Bull.*, vol. 26, no. 3, pp. 341–348, Aug. 1991, doi: 10.1007/BF00587979.
[23] C. L. Tucker III and P. Moldenaers, "Microstructural Evolution in Polymer Blends," *Annu. Rev. Fluid Mech.*, vol. 34, no. 1, pp. 177–210, 2002, doi: 10.1146/annurev.fluid.34.082301.144051.
[24] S. Shen, E. D. Sudol, and M. S. El-Aasser, "Control of particle size in dispersion polymerization of methyl methacrylate," *J. Polym. Sci. Part Polym. Chem.*, vol. 31, no. 6, pp. 1393–1402, 1993, doi: 10.1002/pola.1993.080310606.
[25] D. Li, L. Zhou, X. Wang, L. He, and X. Yang, "Effect of Crystallinity of Polyethylene with Different Densities on Breakdown Strength and Conductance Property," *Materials*, vol. 12, no. 11, Art. no. 11, Jan. 2019, doi: 10.3390/ma12111746.
[26] T. Ahmed and O. Mamat, "The development and characterization of HDPE-silica sand nanoparticles composites," in *2011 IEEE Colloquium on Humanities, Science and Engineering*, Dec. 2011, pp. 6–11. doi: 10.1109/CHUSER.2011.6163824.
[27] A. Z. Samuel, B.-H. Lai, S.-T. Lan, M. Ando, C.-L. Wang, and H. Hamaguchi, "Estimating Percent Crystallinity of Polyethylene as a Function of Temperature by Raman

Spectroscopy Multivariate Curve Resolution by Alternating Least Squares," *Anal. Chem.*, vol. 89, no. 5, pp. 3043–3050, Mar. 2017, doi: 10.1021/acs.analchem.6b04750.
[28] A. Z. Samuel *et al.*, "Determination of Percent Crystallinity of Side-Chain Crystallized Alkylated-Dextran Derivatives with Raman Spectroscopy and Multivariate Curve Resolution," *Anal. Chem.*, vol. 88, no. 9, pp. 4644–4650, May 2016, doi: 10.1021/acs.analchem.5b04075.
[29] P. Rachtanapun, S. E. M. Selke, and L. M. Matuana, "Effect of the high-density polyethylene melt index on the microcellular foaming of high-density polyethylene/polypropylene blends," *J. Appl. Polym. Sci.*, vol. 93, no. 1, pp. 364–371, 2004, doi: 10.1002/app.20428.
[30] B. Hoelzel, B. Herren, M. C. Saha, and Y. Liu, "Investigation of Selective Laser Sintering of High-Density Polyethylene Using Optimized 3D Printing Parameters," presented at the ASME 2021 International Mechanical Engineering Congress and Exposition, Jan. 2022. doi: 10.1115/IMECE2021-70865.
[31] X. Ye, Y. Li, Y. Ai, and Y. Nie, "Novel powder packing theory with bimodal particle size distribution-application in superalloy," *Adv. Powder Technol.*, vol. 29, no. 9, pp. 2280–2287, Sep. 2018, doi: 10.1016/j.apt.2018.06.012.
[32] J. Schmidt *et al.*, "A Novel Process Chain for the Production of Spherical SLS Polymer Powders with Good Flowability," *Procedia Eng.*, vol. 102, pp. 550–556, Dec. 2015, doi: 10.1016/j.proeng.2015.01.123.
[33] R. D. Goodridge, C. J. Tuck, and R. J. M. Hague, "Laser sintering of polyamides and other polymers," *Prog. Mater. Sci.*, vol. 57, no. 2, pp. 229–267, Feb. 2012, doi: 10.1016/j.pmatsci.2011.04.001.
[34] J. P. Schultz, J. P. Martin, R. G. Kander, and C. T. A. Suchicital, "Selective Laser Sintering of Nylon 12-PEEK Blends Formed by Cryogenic Mechanical Alloying," 2000. doi: 10.26153/tsw/3026.
[35] S. Berretta, O. Ghita, and K. E. Evans, "Morphology of polymeric powders in Laser Sintering (LS): From Polyamide to new PEEK powders," *Eur. Polym. J.*, vol. 59, pp. 218–229, Oct. 2014, doi: 10.1016/j.eurpolymj.2014.08.004.
[36] J. Xie, H. Zhang, Y. Shao, D. Bao, H. Zhang, and J. Zhu, "Investigation of the Performance of Fumed Silica as Flow Additive in Polyester Powder Coatings," *Coatings*, vol. 10, no. 10, Art. no. 10, Oct. 2020, doi: 10.3390/coatings10100977.
[37] N. A. Charoo *et al.*, "Selective laser sintering 3D printing – an overview of the technology and pharmaceutical applications," *Drug Dev. Ind. Pharm.*, vol. 46, no. 6, pp. 869–877, Jun. 2020, doi: 10.1080/03639045.2020.1764027.
[38] J. Saroia *et al.*, "A review on 3D printed matrix polymer composites: its potential and future challenges," *Int. J. Adv. Manuf. Technol.*, vol. 106, no. 5, pp. 1695–1721, Jan. 2020, doi: 10.1007/s00170-019-04534-z.
[39] G. Brooks, K. Kinsley, and T. Owens, "3D Printing As A Consumer Technology Business Model," *Int. J. Manag. Inf. Syst. IJMIS*, vol. 18, no. 4, Art. no. 4, Sep. 2014, doi: 10.19030/ijmis.v18i4.8819.
[40] H. N. Chia and B. M. Wu, "Recent advances in 3D printing of biomaterials," *J. Biol. Eng.*, vol. 9, no. 1, p. 4, Mar. 2015, doi: 10.1186/s13036-015-0001-4.
[41] N. Maqsood and M. Rimasauskas, *A Review on Development and Manufacturing of Polymer Matrix Composites Using 3D Printing Technologies*. 2020.

[42] A. Awad, F. Fina, A. Goyanes, S. Gaisford, and A. W. Basit, “3D printing: Principles and pharmaceutical applications of selective laser sintering,” *Int. J. Pharm.*, vol. 586, p. 119594, Aug. 2020, doi: 10.1016/j.ijpharm.2020.119594.
[43] M. Heckele and W. K. Schomburg, “Review on micro molding of thermoplastic polymers,” *J. Micromechanics Microengineering*, vol. 14, no. 3, pp. R1–R14, Mar. 2004, doi: 10.1088/0960-1317/14/3/R01.
[44] M. E. Grigore, “Methods of Recycling, Properties and Applications of Recycled Thermoplastic Polymers,” *Recycling*, vol. 2, no. 4, Art. no. 4, Dec. 2017, doi: 10.3390/recycling2040024.
[45] A. P. da Costa, E. C. Botelho, M. L. Costa, N. E. Narita, and J. R. Tarpani, “A Review of Welding Technologies for Thermoplastic Composites in Aerospace Applications,” *J. Aerosp. Technol. Manag.*, vol. 4, pp. 255–265, Sep. 2012, doi: 10.5028/jatm.2012.04033912.
[46] A. B. Bhattacharya, T. Chatterjee, and K. Naskar, “Automotive applications of thermoplastic vulcanizates,” *J. Appl. Polym. Sci.*, vol. 137, no. 27, p. 49181, 2020, doi: 10.1002/app.49181.
[47] C. C. Ibeh, *Thermoplastic Materials: Properties, Manufacturing Methods, and Applications*. CRC Press, 2011.
[48] M. Wang, L. L. Hench, and W. Bonfield, “Bioglass®/high density polyethylene composite for soft tissue applications: Preparation and evaluation,” *J. Biomed. Mater. Res.*, vol. 42, no. 4, pp. 577–586, 1998, doi: 10.1002/(SICI)1097-4636(19981215)42:4<577::AID-JBM14>3.0.CO;2-2.
[49] W. Xu *et al.*, “3D printing for polymer/particle-based processing: A review,” *Compos. Part B Eng.*, vol. 223, p. 109102, Oct. 2021, doi: 10.1016/j.compositesb.2021.109102.
[50] M. Schmid, A. Amado, and K. Wegener, “Polymer powders for selective laser sintering (SLS),” *AIP Conf. Proc.*, vol. 1664, no. 1, p. 160009, May 2015, doi: 10.1063/1.4918516.
[51] G. Yu, J. Ma, J. Li, J. Wu, J. Yu, and X. Wang, “Mechanical and Tribological Properties of 3D Printed Polyamide 12 and SiC/PA12 Composite by Selective Laser Sintering,” *Polymers*, vol. 14, no. 11, Art. no. 11, Jan. 2022, doi: 10.3390/polym14112167.
[52] S. Song, Y. Li, S. Bai, and Q. Wang, “Production of spherical polymeric composite powder for selective laser sintering via plasma assisted solid state shear milling: From theory to piezoelectric application,” *Chem. Eng. J.*, vol. 415, p. 129035, Jul. 2021, doi: 10.1016/j.cej.2021.129035.
[53] M. Schmid and K. Wegener, “Additive Manufacturing: Polymers Applicable for Laser Sintering (LS),” *Procedia Eng.*, vol. 149, pp. 457–464, Jan. 2016, doi: 10.1016/j.proeng.2016.06.692.
[54] D. M. Bigg, “Mechanical property enhancement of semicrystalline polymers—A review,” *Polym. Eng. Sci.*, vol. 28, no. 13, pp. 830–841, 1988, doi: 10.1002/pen.760281303.
[55] S. Aggarwal, M. Sajwan, and R. B. Singh, “CRYSTALLINITY OF HDPE PIPES BY DSC, XRD AND FTIRSPECTROSCOPY-A FORENSIC COMPARISON,” *Indian J. Criminol. Crim.*, vol. 29, no. 2, pp. 141–148, May 2008.
[56] F. Benabid, N. Kharchi, F. Zouai, A.-H. I. Mourad, and D. Benachour, “Impact of co-mixing technique and surface modification of ZnO nanoparticles using stearic acid on their dispersion into HDPE to produce HDPE/ZnO nanocomposites,” *Polym. Polym. Compos.*, vol. 27, no. 7, pp. 389–399, 2019, doi: 10.1177/0967391119847353.

[57] N. B. R. Kumar, V. Crasta, and B. M. Praveen, “Advancement in Microstructural, Optical, and Mechanical Properties of PVA (Mowiol 10-98) Doped by ZnO Nanoparticles,” *Phys. Res. Int.*, vol. 2014, p. 9, 2014, doi: 10.1155/2014/742378.
[58] E. B. Mejia *et al.*, “Impact on HDPE Mechanical Properties and Morphology due to Processing,” in *2019 Advances in Science and Engineering Technology International Conferences (ASET)*, Mar. 2019, pp. 1–5. doi: 10.1109/ICASET.2019.8714456.
[59] M. Xie, J. Chen, and H. Li, “Morphology and mechanical properties of injection-molded ultrahigh molecular weight polyethylene/polypropylene blends and comparison with compression molding,” *J. Appl. Polym. Sci.*, vol. 111, no. 2, pp. 890–898, 2009, doi: 10.1002/app.29036.
[60] A. D. Valino, J. R. C. Dizon, A. H. Espera, Q. Chen, J. Messman, and R. C. Advincula, “Advances in 3D printing of thermoplastic polymer composites and nanocomposites,” *Prog. Polym. Sci.*, vol. 98, p. 101162, Nov. 2019, doi: 10.1016/j.progpolymsci.2019.101162.
[61] Y. Zhang, L. Hao, M. M. Savalani, R. A. Harris, and K. E. Tanner, “Characterization and dynamic mechanical analysis of selective laser sintered hydroxyapatite-filled polymeric composites,” *J. Biomed. Mater. Res. A*, vol. 86A, no. 3, pp. 607–616, 2008, doi: 10.1002/jbm.a.31622.
[62] J. W. Stansbury and M. J. Idacavage, “3D printing with polymers: Challenges among expanding options and opportunities,” *Dent. Mater.*, vol. 32, no. 1, pp. 54–64, Jan. 2016, doi: 10.1016/j.dental.2015.09.018.
[63] A. A. Zhansitov *et al.*, “Synthesis and Properties of Polyetheretherketones for 3D Printing,” *Fibre Chem.*, vol. 49, no. 6, pp. 414–419, Mar. 2018, doi: 10.1007/s10692-018-9911-5.
[64] F. Fina, A. Goyanes, S. Gaisford, and A. W. Basit, “Selective laser sintering (SLS) 3D printing of medicines,” *Int. J. Pharm.*, vol. 529, no. 1, pp. 285–293, Aug. 2017, doi: 10.1016/j.ijpharm.2017.06.082.
[65] C. Hong, X. Wang, K. Han, D. Su, and Z. Chen, “Performance investigation of 3D printed clay soil using fiber Bragg grating technology,” *Acta Geotech.*, vol. 17, no. 2, pp. 453–462, Feb. 2022, doi: 10.1007/s11440-021-01250-5.
[66] C. F. Revelo and H. A. Colorado, “3D printing of kaolinite clay ceramics using the Direct Ink Writing (DIW) technique,” *Ceram. Int.*, vol. 44, no. 5, pp. 5673–5682, Apr. 2018, doi: 10.1016/j.ceramint.2017.12.219.
[67] M. Li *et al.*, “Lightweight mullite ceramics with controlled porosity and enhanced properties prepared by SLS using mechanical mixed FAHSs/polyamide12 composites,” *Ceram. Int.*, vol. 45, no. 16, pp. 20803–20809, Nov. 2019, doi: 10.1016/j.ceramint.2019.07.067.
[68] X. Liu, B. Zou, H. Xing, and C. Huang, “The preparation of ZrO2-Al2O3 composite ceramic by SLA-3D printing and sintering processing,” *Ceram. Int.*, vol. 46, no. 1, pp. 937–944, Jan. 2020, doi: 10.1016/j.ceramint.2019.09.054.
[69] W. Du, X. Ren, Z. Pei, and C. Ma, “Ceramic Binder Jetting Additive Manufacturing: A Literature Review on Density,” *J. Manuf. Sci. Eng.*, vol. 142, no. 4, Feb. 2020, doi: 10.1115/1.4046248.
[70] H. Fayazfar, F. Liravi, U. Ali, and E. Toyserkani, “Additive manufacturing of high loading concentration zirconia using high-speed drop-on-demand material jetting,” *Int. J.*

Adv. Manuf. Technol., vol. 109, no. 9, pp. 2733–2746, Aug. 2020, doi: 10.1007/s00170-020-05829-2.
[71] S. M. Gaytan *et al.*, "Fabrication of barium titanate by binder jetting additive manufacturing technology," *Ceram. Int.*, vol. 41, no. 5, Part A, pp. 6610–6619, Jun. 2015, doi: 10.1016/j.ceramint.2015.01.108.
[72] H. Qu, "Additive manufacturing for bone tissue engineering scaffolds," *Mater. Today Commun.*, vol. 24, p. 101024, Sep. 2020, doi: 10.1016/j.mtcomm.2020.101024.
[73] A. Renteria *et al.*, "Direct ink write multi-material printing of PDMS-BTO composites with MWCNT electrodes for flexible force sensors," *Flex. Print. Electron.*, vol. 7, no. 1, p. 015001, Jan. 2022, doi: 10.1088/2058-8585/ac442e.
[74] W. Li, A. Ghazanfari, D. McMillen, M. C. Leu, G. E. Hilmas, and J. Watts, "Fabricating ceramic components with water dissolvable support structures by the Ceramic On-Demand Extrusion process," *CIRP Ann.*, vol. 66, no. 1, pp. 225–228, Jan. 2017, doi: 10.1016/j.cirp.2017.04.129.
[75] A. Renteria *et al.*, "Influence of bimodal particle distribution on material properties of BaTiO3 fabricated by paste extrusion 3D printing," *Ceram. Int.*, vol. 47, no. 13, pp. 18477–18486, Jul. 2021, doi: 10.1016/j.ceramint.2021.03.171.
[76] S. S. L. Chan, R. M. Pennings, L. Edwards, and G. V. Franks, "3D printing of clay for decorative architectural applications: Effect of solids volume fraction on rheology and printability," *Addit. Manuf.*, vol. 35, p. 101335, Oct. 2020, doi: 10.1016/j.addma.2020.101335.
[77] K. Faksawat, P. Limsuwan, and K. Naemchanthara, "3D printing technique of specific bone shape based on raw clay using hydroxyapatite as an additive material," *Appl. Clay Sci.*, vol. 214, p. 106269, Nov. 2021, doi: 10.1016/j.clay.2021.106269.
[78] A. Wolf, P. L. Rosendahl, and U. Knaack, "Additive manufacturing of clay and ceramic building components," *Autom. Constr.*, vol. 133, p. 103956, Jan. 2022, doi: 10.1016/j.autcon.2021.103956.
[79] M. Peroglio, C. Meunier, J. Favre, J. Faucheu, and C. Petit, "A parametric study of conventional and high-speed microwave sintering of robocast porcelain," *Open Ceram.*, vol. 9, p. 100246, Mar. 2022, doi: 10.1016/j.oceram.2022.100246.
[80] L. R. Sbriglia, A. M. Baker, J. M. Thompson, R. V. Morgan, A. J. Wachtor, and J. D. Bernardin, "Embedding Sensors in FDM Plastic Parts During Additive Manufacturing," in *Topics in Modal Analysis & Testing, Volume 10*, Cham, 2016, pp. 205–214. doi: 10.1007/978-3-319-30249-2_17.
[81] G. Stano, S. M. A. I. Ovy, J. R. Edwards, M. Cianchetti, G. Percoco, and Y. Tadesse, "One-shot additive manufacturing of robotic finger with embedded sensing and actuation," *Int. J. Adv. Manuf. Technol.*, vol. 124, no. 1, pp. 467–485, Jan. 2023, doi: 10.1007/s00170-022-10556-x.
[82] D. Lehmhus *et al.*, "Customized Smartness: A Survey on Links between Additive Manufacturing and Sensor Integration," *Procedia Technol.*, vol. 26, pp. 284–301, Jan. 2016, doi: 10.1016/j.protcy.2016.08.038.
[83] H. Liu *et al.*, "3D Printed Flexible Strain Sensors: From Printing to Devices and Signals," *Adv. Mater.*, vol. 33, no. 8, p. 2004782, 2021, doi: 10.1002/adma.202004782.
[84] J. A. Lewis, "Direct Ink Writing of 3D Functional Materials," *Adv. Funct. Mater.*, vol. 16, no. 17, pp. 2193–2204, 2006, doi: 10.1002/adfm.200600434.

[85] A. Shahzad and I. Lazoglu, “Direct ink writing (DIW) of structural and functional ceramics: Recent achievements and future challenges,” *Compos. Part B Eng.*, vol. 225, p. 109249, Nov. 2021, doi: 10.1016/j.compositesb.2021.109249.
[86] L. del-Mazo-Barbara and M.-P. Ginebra, “Rheological characterisation of ceramic inks for 3D direct ink writing: A review,” *J. Eur. Ceram. Soc.*, vol. 41, no. 16, pp. 18–33, Dec. 2021, doi: 10.1016/j.jeurceramsoc.2021.08.031.
[87] N. Cruz and Y. Peng, “Rheology measurements for flotation slurries with high clay contents – A critical review,” *Miner. Eng.*, vol. 98, pp. 137–150, Nov. 2016, doi: 10.1016/j.mineng.2016.08.011.
[88] A. Karamanov, E. Karamanova, A. M. Ferrari, F. Ferrante, and M. Pelino, “The effect of fired scrap addition on the sintering behaviour of hard porcelain,” *Ceram. Int.*, vol. 32, no. 7, pp. 727–732, Jan. 2006, doi: 10.1016/j.ceramint.2005.05.009.
[89] O. I. Ece and Z. Nakagawa, “Bending strength of porcelains,” *Ceram. Int.*, vol. 28, no. 2, pp. 131–140, Jan. 2002, doi: 10.1016/S0272-8842(01)00068-2.
[90] S. M. Olhero, G. Tarì, and J. M. F. Ferreira, “Feedstock Formulations for Direct Consolidation of Porcelains with Polysaccharides,” *J. Am. Ceram. Soc.*, vol. 84, no. 4, pp. 719–725, 2001, doi: 10.1111/j.1151-2916.2001.tb00732.x.
[91] K. Jeoung-Ah, “The characterisation of paper composite porcelain in a fired state by XRD and SEM,” *J. Eur. Ceram. Soc.*, vol. 24, no. 15, pp. 3823–3831, Dec. 2004, doi: 10.1016/j.jeurceramsoc.2004.03.002.
[92] M. Banno, T. Tanaka, T. Nishikawa, and Y. Kitamura, “Improvement in Flexural Strength of Porcelain Bodies by Applying Surface Compressive Stress,” *J. Ceram. Soc. Jpn.*, vol. 114, no. 1328, pp. 329–331, 2006, doi: 10.2109/jcersj.114.329.
[93] S. D. Savage, M. A. Wilson, M. A. Carter, W. D. Hoff, C. Hall, and B. McKay, “Moisture expansion and mass gain in fired clay ceramics: a two-stage (time)$\less$sup$\greater$1/4$\less$/sup$\greater$process,” *J. Phys. Appl. Phys.*, vol. 41, no. 5, p. 055402, Feb. 2008, doi: 10.1088/0022-3727/41/5/055402.
[94] O. Al-Shantir, M. Keppert, M. Vrabec, and A. Trník, “Influence of compression pressure on thermal expansion, bulk density, and porosity of electroporcelain after firing,” *AIP Conf. Proc.*, vol. 2275, no. 1, p. 020001, Sep. 2020, doi: 10.1063/5.0025878.
[95] H. C. Tsai, K. Chen, Y. Liu, J. P. Norair, S. Bellamy, and J. Shuler, “Applying RFID technology in nuclear materials management,” *Packag. Transp. Storage Secur. Radioact. Mater.*, vol. 19, no. 1, pp. 41–46, Mar. 2008, doi: 10.1179/174651008X279000.
[96] “Performance of Embedded Sensors in 3D Printed SiC... | ORNL.” https://www.ornl.gov/publication/performance-embedded-sensors-3d-printed-sic (accessed Nov. 01, 2022).
[97] K. V. Wong and A. Hernandez, “A Review of Additive Manufacturing,” *Int. Sch. Res. Netw.*, vol. 2012, p. 10, Jun. 2012, doi: doi:10.5402/2012/208760.
[98] M. Attaran, “The rise of 3-D printing: The advantages of additive manufacturing over traditional manufacturing,” *Bus. Horiz.*, vol. 60, no. 5, pp. 677–688, Sep. 2017, doi: 10.1016/j.bushor.2017.05.011.
[99] L. L. Lopez Taborda, H. Maury, and J. Pacheco, “Design for additive manufacturing: a comprehensive review of the tendencies and limitations of methodologies,” *Rapid Prototyp. J.*, vol. 27, no. 5, pp. 918–966, Jan. 2021, doi: 10.1108/RPJ-11-2019-0296.
[100] F. J. Lino Alves, A. M. Baptista, and A. T. Marques, “3 - Metal and ceramic matrix composites in aerospace engineering,” in *Advanced Composite Materials for Aerospace*

Engineering, S. Rana and R. Fangueiro, Eds. Woodhead Publishing, 2016, pp. 59–99. doi: 10.1016/B978-0-08-100037-3.00003-1.
[101] T. Masumoto and K. Hashimoto, "Chemical Properties of Amorphous Metals," *Annu. Rev. Mater. Sci.*, vol. 8, no. 1, pp. 215–233, Aug. 1978, doi: 10.1146/annurev.ms.08.080178.001243.
[102] S. Singh, G. Singh, C. Prakash, and S. Ramakrishna, "Current status and future directions of fused filament fabrication," *J. Manuf. Process.*, vol. 55, pp. 288–306, Jul. 2020, doi: 10.1016/j.jmapro.2020.04.049.
[103] N. Mohan, P. Senthil, S. Vinodh, and N. Jayanth, "A review on composite materials and process parameters optimisation for the fused deposition modelling process," *Virtual Phys. Prototyp.*, vol. 12, no. 1, pp. 47–59, Jan. 2017, doi: 10.1080/17452759.2016.1274490.
[104] S. Singh and R. Singh, "Wear modelling of Al-Al2O3 functionally graded material prepared by FDM assisted investment castings using dimensionless analysis," *J. Manuf. Process.*, vol. 20, pp. 507–514, Oct. 2015, doi: 10.1016/j.jmapro.2015.01.007.
[105] S. H. Masood and W. Q. Song, "Thermal characteristics of a new metal/polymer material for FDM rapid prototyping process," *Assem. Autom.*, vol. 25, no. 4, pp. 309–315, Jan. 2005, doi: 10.1108/01445150510626451.
[106] S. Kumar and J.-P. Kruth, "Composites by rapid prototyping technology," *Mater. Des.*, vol. 31, no. 2, pp. 850–856, Feb. 2010, doi: 10.1016/j.matdes.2009.07.045.
[107] S. Singh, S. Ramakrishna, and R. Singh, "Material issues in additive manufacturing: A review," *J. Manuf. Process.*, vol. 25, pp. 185–200, Jan. 2017, doi: 10.1016/j.jmapro.2016.11.006.
[108] O. Miclette, R. Côté, V. Demers, and V. Brailovski, "Material extrusion additive manufacturing of low-viscosity metallic feedstocks: Performances of the plunger-based approach," *Addit. Manuf.*, vol. 60, p. 103252, Dec. 2022, doi: 10.1016/j.addma.2022.103252.
[109] J. Gonzalez-Gutierrez, F. Arbeiter, T. Schlauf, C. Kukla, and C. Holzer, "Tensile properties of sintered 17-4PH stainless steel fabricated by material extrusion additive manufacturing," *Mater. Lett.*, vol. 248, pp. 165–168, Aug. 2019, doi: 10.1016/j.matlet.2019.04.024.
[110] F.-F. Li *et al.*, "SiC ceramic mirror fabricated by additive manufacturing with material extrusion and laser cladding," *Addit. Manuf.*, vol. 58, p. 102994, Oct. 2022, doi: 10.1016/j.addma.2022.102994.
[111] H. Hur, Y. Jin Park, D.-H. Kim, and J. Wan Ko, "Material extrusion for ceramic additive manufacturing with polymer-free ceramic precursor binder," *Mater. Des.*, vol. 221, p. 110930, Sep. 2022, doi: 10.1016/j.matdes.2022.110930.
[112] D. Han and H. Lee, "Recent advances in multi-material additive manufacturing: methods and applications," *Curr. Opin. Chem. Eng.*, vol. 28, pp. 158–166, Jun. 2020, doi: 10.1016/j.coche.2020.03.004.
[113] H. Nassar, M. Ntagios, W. T. Navaraj, and R. Dahiva, "Multi-Material 3D Printed Bendable Smart Sensing Structures," in *2018 IEEE SENSORS*, Oct. 2018, pp. 1–4. doi: 10.1109/ICSENS.2018.8589625.
[114] T. Hainsworth, L. Smith, S. Alexander, and R. MacCurdy, "A Fabrication Free, 3D Printed, Multi-Material, Self-Sensing Soft Actuator," *IEEE Robot. Autom. Lett.*, vol. 5, no. 3, pp. 4118–4125, Jul. 2020, doi: 10.1109/LRA.2020.2986760.

[115] B. Shih *et al.*, “Design Considerations for 3D Printed, Soft, Multimaterial Resistive Sensors for Soft Robotics,” *Front. Robot. AI*, vol. 6, 2019, Accessed: Mar. 06, 2023. [Online]. Available: https://www.frontiersin.org/articles/10.3389/frobt.2019.00030
[116] J. Brackett *et al.*, “The Impact of Material Extrusion 3d Print Parameters on Porosity and Tensile Properties.” Rochester, NY, Apr. 21, 2022. doi: 10.2139/ssrn.4089333.
[117] C. Bellehumeur, L. Li, Q. Sun, and P. Gu, “Modeling of Bond Formation Between Polymer Filaments in the Fused Deposition Modeling Process,” *J. Manuf. Process.*, vol. 6, no. 2, pp. 170–178, 2004.
[118] C. Ziemian, M. Sharma, and S. Ziemian, “Anisotropic Mechanical Properties of ABS Parts Fabricated by Fused Deposition Modelling,” *Mech. Eng.*, Apr. 2012, [Online]. Available: https://digitalcommons.bucknell.edu/fac_books/72
[119] J. F. Rodríguez, J. P. Thomas, and J. E. Renaud, “Mechanical behavior of acrylonitrile butadiene styrene fused deposition materials modeling,” *Rapid Prototyp. J.*, vol. 9, no. 4, pp. 219–230, Jan. 2003, doi: 10.1108/13552540310489604.
[120] M. P. Serdeczny, R. Comminal, D. B. Pedersen, and J. Spangenberg, “Numerical simulations of the mesostructure formation in material extrusion additive manufacturing,” *Addit. Manuf.*, vol. 28, pp. 419–429, Aug. 2019, doi: 10.1016/j.addma.2019.05.024.
[121] C. Tosto, J. Tirillò, F. Sarasini, and G. Cicala, “Hybrid Metal/Polymer Filaments for Fused Filament Fabrication (FFF) to Print Metal Parts,” *Appl. Sci.*, vol. 11, no. 4, Art. no. 4, Jan. 2021, doi: 10.3390/app11041444.
[122] J. Butt and R. Bhaskar, “Investigating the Effects of Annealing on the Mechanical Properties of FFF-Printed Thermoplastics,” *J. Manuf. Mater. Process.*, vol. 4, no. 2, Art. no. 2, Jun. 2020, doi: 10.3390/jmmp4020038.
[123] L. Xinhua, L. Shengpeng, L. Zhou, Z. Xianhua, C. Xiaohu, and W. Zhongbin, “An investigation on distortion of PLA thin-plate part in the FDM process,” *Int. J. Adv. Manuf. Technol.*, vol. 79, no. 5, pp. 1117–1126, Jul. 2015, doi: 10.1007/s00170-015-6893-9.
[124] S. Manzari, C. Occhiuzzi, S. Nawale, A. Catini, C. Di Natale, and G. Marrocco, “Humidity Sensing by Polymer-Loaded UHF RFID Antennas,” *IEEE Sens. J.*, vol. 12, no. 9, pp. 2851–2858, Sep. 2012, doi: 10.1109/JSEN.2012.2202897.
[125] U. K. Roopavath, S. Malferrari, A. Van Haver, F. Verstreken, S. N. Rath, and D. M. Kalaskar, “Optimization of extrusion based ceramic 3D printing process for complex bony designs,” *Mater. Des.*, vol. 162, pp. 263–270, Jan. 2019, doi: 10.1016/j.matdes.2018.11.054.

Vita

Cory Marquez served four years active duty in the United States Marine Corps with the 1st Combat Engineer Battalion, 1st Marine Division in Camp Pendleton, CA. Cory honorably discharged in 2015 and enrolled in community college in summer of 2016. Cory holds an associate degree in Mechanical Engineering and Multidisciplinary Studies from El Paso Community College. Later, Cory transferred to The University of Texas at El Paso where he obtained his Bachelor of Science in Mechanical Engineering. Later, he went straight into the Ph.D. Mechanical Engineering program where he managed to obtain a Master of Science in Mechanical Engineering and Graduate Certification in 3D Engineering and Additive Manufacturing. During his time in his doctoral program, Cory has one first author paper in submission for publication and three first author pending papers for submission for publication. Cory also is co-author of five journal publications.

Contact Information: cmarquez10@miners.utep.edu